IMPACTS OF MINERAL SURFACE REACTIONS ON AQUEOUS VANADATE ATTENUATION

A Thesis Submitted to the College of

Graduate and Postdoctoral Studies

In Partial Fulfillment of the Requirements

For the Degree of Master of Science

In the Department of Geological Sciences

University of Saskatchewan

Saskatoon

By

COLTON JAMES VESSEY

PERMISSION TO USE

In presenting this thesis in partial fulfillment of the requirements for a Postgraduate degree from the University of Saskatchewan, I agree that the Libraries of this University may make it freely available for inspection. I further agree that permission for copying of this thesis in any manner, in whole or in part, for scholarly purposes may be granted by the professor or professors who supervised my thesis work or, in their absence, by the Head of the Department or the Dean of the College in which my thesis work was done. It is understood that any copying or publication or use of this thesis or parts thereof for financial gain shall not be allowed without my written permission. It is also understood that due recognition shall be given to me and to the University of Saskatchewan in any scholarly use which may be made of any material in my thesis.

Requests for permission to copy or to make other uses of materials in this thesis/dissertation in whole or part should be addressed to:

Head of the Department of Geological Sciences
114 Science Place
University of Saskatchewan
Saskatoon, Saskatchewan S7N 5E2 Canada

Dean

College of Graduate and Postdoctoral Studies

University of Saskatchewan

116 Thorvaldson Building, 110 Science Place

Saskatoon, Saskatchewan S7N 5C9 Canada

ABSTRACT

Accumulation of vanadium (V) in the environment has become a global concern due to increased anthropogenic activity. Release of V by fossil fuel emissions or leaching of mine waste materials can concentrate V in aquatic systems, where it may reach concentrations hazardous to organisms and humans. Similar to potentially-hazardous elements (e.g., Mo and W), V is a redox-sensitive trace metal that predominantly occurs in three oxidation states (+III, +IV, and +V) in near-surface environments. Therefore, pH, redox conditions, and V concentration ($[V]_T$) strongly affect aqueous speciation and attenuation mechanisms at mineral surfaces. Adsorption onto Fe (oxyhydr)oxides and Fe sulfides are key controls on metal(loid) mobility in terrestrial and marine environments. However, few studies have examined fundamental attenuation mechanisms for V within these systems. The objective of this thesis is to determine rates and mechanisms of V adsorption and, more generally, to improve understanding of environmental V geochemistry. Laboratory experiments examined (i) potential for aqueous vanadate ($H_2V^VO_4^-$) removal by Fe(II)-bearing phases (i.e., magnetite, mackinawite, siderite, and pyrite) under anoxic conditions and (ii) uptake of polynuclear V(V) species by Fe(III) (oxyhydr)oxides. Kinetic batch experiments demonstrated the rapid uptake of V under anoxic conditions by siderite and mackinawite (≥ 90 %) after 3 h, whereas removal by magnetite reached ~50 % and was limited during reaction with pyrite. Further XAS analysis showed the reduction of V(V) to V(IV) and V(III) with the formation of bidentate edge- and corner-sharing surface complexes at magnetite, while only bidentate binuclear surface complexes were observed following reaction with siderite. In the case of mackinawite, data suggests the incorporation of V(IV) and V(III) into the tetragonal FeS structure. Investigation of (poly)vanadate adsorption at ferrihydrite and hematite surfaces was performed using *in situ* attenuated total reflectance – Fourier transform infrared spectroscopy. Results highlight the pH dependency of polymerization reactions and, consequently, the formation of surface polymers. Ferrihydrite exhibited limited capacity for polyvanadate uptake at pH 5 and 6, whereas polymers had a high affinity for hematite from pH 3 to 6. Overall, this research improves understanding of relationships between metal-mineral interactions, redox conditions, and aqueous speciation reactions that influence V mobility in natural and contaminated environments.

ACKNOWLEDGEMENTS

I would first like to thank my supervisor and mentor Dr. Matthew Lindsay. Thank you for the many academic and professional development opportunities you have given me throughout my time with your group. I am also extremely grateful for your invaluable contribution to my growth as a researcher and to my career. I would also like to thank Dr. Jared Robertson for his patience and guidance in teaching me much of what I know about XAS and synchrotron science. I also want to acknowledge Dr. Bruce Eglington, Dr. Joyce McBeth, Dr. Soumya Das, Dr. Derek Peak, and Dr. Michael Schmidt for teaching me various aspects in Earth Science.

My eternal thanks to everyone in the Environmental Geochemistry Research Group throughout my time at USask, especially: Mattea Cowell, Aidan Mowat, Noel Galuschik, Mojtaba Abdolahnezhad, Carlo Cilia, Sarah Rudderham. I also want to thank the commissioner of the Lindsay lab duck hunting committee, Lawrence Swerhone, and its other founding members, James Schulte and Daniel Francis, for their support and friendship. I would also like to acknowledge the University of Saskatchewan Geological Sciences staff, especially Dr. Jing Chen for performing water analyses and her patience in developing the HPLC-ICP-MS method.

Thank you to the University of Saskatchewan and NSERC for providing funding which made this project possible.

I am especially grateful to my family and friends for their unconditional support. To my wonderful fiancée, Deanna, thank you for your love and encouragement throughout this entire thesis.

Lastly, to my grandmother Rose Koberinski - thank you for your patience and love throughout the entirety of my post-secondary education. My educational journey would not have been possible without you.

TABLE OF CONTENTS

LIST OF TABLES

LIST OF FIGURES

LIST OF ABBREVIATIONS

σ^2	Debye-Waller factor (Å2)
χ^2_{red}	Reduced chi-square
ATR-FTIR	Attenuated total reflectance-Fourier transform infrared
BET	Brunauer-Emmet-Teller
CLS	Canadian Light Source
CMCF	Canadian Light Source Canadian Macromolecular Crystallography Facility
CN	Coordination number
ΔE	Energy shift (eV)
EXAFS	Extended X-ray absorption fine structure
EDX	Energy dispersive X-ray
Fh	Ferrihydrite
HDPE	High-density polyethylene
ICP-MS	Inductively coupled plasma mass spectrometry
IRE	Internal reflective element
k	Photoelectron wave vector
K	Partitioning coefficient
k_b	Reverse reaction rate constant
K_{eq}	Equilibrium rate constant
k_f	Forward reaction rate constant
k_i	Irreversible reaction rate constant
R	Interatomic distance
RMSE	Root mean square error

Mag	Magnetite
Mck	Mackinawite
MOPS	3-morpholinopropane-1-sulfonic acid buffer
pH_{PZC}	pH point of zero charge
PTFE	Polytetrafluoroethylene
Py	Pyrite
S_0^2	Amplitude reduction factor
Sd	Siderite
SSA	Specific surface area
SXRMB	Canadian Light Source Soft X-ray Microcharacterization Beamline
TEM	Transmission electron microscopy – energy dispersive X-ray spectroscopy
$[V]_T$	Total vanadium concentration
XANES	X-ray absorption near edge structure
XAS	X-ray absorption spectroscopy
XRD	X-ray diffraction

CHAPTER 1: INTROUCTION

Vanadium (V) is a reduction-oxidation (redox) sensitive trace metal that naturally occurs in a range of oxidation states, which has been utilized in industrial activities (i.e., catalytic chemistry, and steel works), as well as studying biogeochemical processes over geologic time scales (Huang et al., 2015; Shaheen et al., 2019; Tribovillard et al., 2006; Wanty and Goldhaber, 1992). Due to recent global anthropogenic release, V has recently gained interest due its complex biogeochemistry and acute toxicity (Aureliano and Crans, 2009; Gustafsson, 2019; Schlesinger et al., 2017; Watt et al., 2018). Like other oxyanion forming metal(loid)s (e.g., As, Cr, and Se), V is an oxyanion-forming element with the potential to form aqueous polynuclear species and has been is listed on the United Sates Environment Protection Agency candidate contaminant list (USEPA, 2016).

Naturally substituting into crystal structures average crustal V concentrations are ~275 mg kg^{-1}; however, this value varies depending on local weathering rates and source material. For example, V concentrations can reach upward of 10,000 mg kg^{-1} in bauxite, phosphate, black shale, and crude oil, and coal deposits (Hobson et al., 2018; Huang et al., 2015; Zubot et al., 2012). While aqueous V concentrations in natural environments generally range between 0.005 to 180 µg L^{-1}, due to weathering of geogenic materials, concentrations exceeding 3 mg L^{-1} have been reporting as a result of industrial activity and waste disposal (Burke et al., 2012; Hudson-Edwards et al., 2019; Nesbitt et al., 2017; Watt et al., 2018). Compared to other metal(loid) species, V geochemical pathways remain poorly constrained, raising concerns regarding its mobility and bioavailability in natural and contaminated systems (Huang et al., 2015; Shaheen et al., 2019; Watt et al., 2018).

Chemical (redox) speciation and adsorption reactions are known to be a dominant control on metal(loid) mobility (e.g., As, Cr, and Se), yet few studies have analyzed the chemical pathways influencing V mobility (Larsson et al., 2017; Peacock and Sherman, 2004; Wanty and Goldhaber, 1992; White and Peterson, 1996). The overall objective of this research is to improve understanding of V geochemistry at water-mineral interfaces by: (i) observing reactions between bioavailable vanadate ($[H_xV^VO_4]^{(3-x)-}$) and Fe(II) bearing minerals, such as pyrite [FeS_2],

mackinawite [FeS], siderite [$FeCO_3$] and magnetite [Fe_3O_4], under anoxic conditions to promote V attenuation through sorption and reduction pathways, and (ii) analyzing uptake mechanisms of polynuclear V species and the potential for surface polymer formation at ferrihydrite [$5Fe_2O_3 \cdot 9H_2O$] and hematite [Fe_2O_3] surfaces.

1.1. Research Hypothesis and Objectives

This thesis examines removal rates and mechanisms of aqueous V(V) (polynuclear) species during surface complexation reactions with Fe(II) and Fe(III) phases.

Hypothesis 1: Under anoxic conditions, Fe(II)-bearing phases (i.e., magnetite, siderite, mackinawite and pyrite) have the potential to adsorb and reduce vanadate to V(IV) or V(III). The specific objectives of this study are:

- Objective 1a: constrain rates and mechanisms for V(V) attenuation under anoxic conditions; and,
- Objective 1b: determine reduction pathways of V(V) during interaction with Fe(II) bearing phases.

Hypothesis 2: Ferrihydrite and hematite have the capacity to adsorb (poly)vanadate species and mediate the formation of surface polymers. The specific objectives of this study are:

- Objective 2a: comparatively analyze pH- and concentration-dependent V(V) uptake at ferrihydrite and hematite surfaces; and,
- Objective 2b: determine bonding mechanisms of (poly)vanadate and the potential for Fe(III) (oxyhydr)oxides surfaces to enhance surface polymer formation using *in* situ attenuated total reflectance-Fourier infrared spectroscopy (ATR-FTIR).

1.2. Thesis Organization

This manuscript-style thesis consists of two research papers (Chapters 3, 4), plus a general introduction (Chapter 1), literature review (Chapter 2), and summary (Chapter 5). The first research paper (Chapter 3) analyzes the capacity for Fe(II)-bearing phases to adsorb and reduce bioavailable vanadate to less mobile V(IV) and V(III) species. Following the study conducted in Chapter 3, questions arose in connection with polynuclear V species adsorption processes at Fe

mineral surfaces and the influence these species may have on inhibiting further metal uptake. These processes for V polymers have yet to be described at Fe(III) (oxyhydr)oxide surfaces. Therefore, the second manuscript (Chapter 4) addresses adsorption mechanisms of (poly)vanadate species from pH 3 to 6 onto ferrihydrite and hematite surfaces using *in situ* ATR-FTIR spectroscopy. ATR-FTIR spectroscopy has the capability to observe molecular-level adsorption mechanisms at liquid-mineral interfaces, and therefore, is a practical method for *in situ* metal experiments. Results from Chapter 3 and 4 address environmentally relevant geochemical reactions pertinent to V attenuation and its overall bioavailability.

CHAPTER 2: LITERATURE REVIEW

2.1. Vanadium Sources

Vanadium release to the terrestrial and marine systems is dependent on biogeochemical processes at mineral surfaces. The average crustal abundance of V ranges between 5 and 300 mg kg^{-1}, and higher concentrations are typically associated with mafic rocks due to V(III) substitution in primary mineral lattices (Huang et al., 2015; Hurlbut and Klein, 1977). Secondary mineral weathering products including clays (kaolinite, illite, chlorite, and smectites) and Al (hydr)oxides can incorporate V(IV) (as VO^{2+}) through substitution into Al(III) octahedral sites (Gehring et al., 1993; Wisawapipat and Kretzschmar, 2017). Similarly, V(III) can substitute for Fe(III) in octahedral sites within goethite due to comparable atomic charge and radius (Kaur et al., 2009; Schwertmann and Pfab, 1994). Vanadium is also incorporated directly into uranium and phosphate minerals, such as carnotite [$K_2(UO_2)(VO_4)_2 \cdot 3H_2O$] or hewettite [$CaV_6O_{16} \cdot 9H_2O$] that are commonly found in tabular and roll front uranium deposits (Cannon, 1952). Vanadium concentrations up to 16,000 mg kg^{-1} can occur in petroleum (i.e., crude oil, carbonaceous black shales) and coal deposits, and in subsequent waste products (e.g., petroleum coke) where V is mainly associated with organic fractions and clay minerals (López et al., 2015; Moskalyk and Alfantazi, 2003; Nesbitt and Lindsay, 2017; Sia and Abdullah, 2011; Zubot et al., 2012). The preservation of V(IV) in organic sediments as VO^{2+}, is due to tetrapyrrole porphyrin structures forming strong bonds that are not disturbed during lithification processes in marine sediments (Lewan, 1984).

2.2. Environmental Toxicology

Terrestrial and marine waters generally exhibit V concentrations range from 0.005 to 180 µg L^{-1}, yet concentrations exceeding 3 mg L^{-1} may result from V leaching from waste materials generated at oil sands, coal, bauxite, uranium, and phosphate mines (Burke et al., 2012; Huang et al., 2015; Hudson-Edwards et al., 2019; Nesbitt and Lindsay, 2017; Shiller and Boyle, 1987). At elevated concentrations, (poly)vanadate species including $[H_xVO_4]^{(3-x)-}$, $[H_xV_2O_7]^{(4-x)-}$, $V_4O_{12}^{4-}$, and $[H_xV_{10}O_{28}]^{(6-x)-}$ are acutely toxic to aquatic organisms (Puttaswamy et al., 2010;

Puttaswamy and Liber, 2011), bacteria (Larsson et al., 2013), and humans (Rehder, 2015; Seargeant and Stinson, 1979) due to their similarity to phosphate inhibiting Ca-, Na-, K-ATPase ion pumps and uptake into cells through ion mimicry of phosphate ligands (Aureliano et al., 2013; Aureliano and Crans, 2009; Crans et al., 2004). While V is included on the USEPA contaminant candidate list, few jurisdictions have established soil or water quality guidelines for this potentially-hazardous metal (Canadian Council of Ministers of the Environment, 1999; Environment and Climate Change Canada, 2016; RIVM Letter Report 601714021/2012; National Institute for Public Health and the Environment, 2012; USEPA, 2016). Canada has established soil criteria for V at 130 mg kg^{-1} (CCME, 1999), and water quality guidelines at 120 µg L^{-1} and 5 µg L^{-1} for freshwater and marine waters, respectively (Environment and Climate Change Canada, 2016). However, recent research has identified a hazardous concentration endangering 5% of species (HC5) to be 50 µg L^{-1} for freshwater aquatic organisms (Schiffer and Liber, 2017).

2.3. Aqueous Speciation

Vanadium mobility in aqueous environments is controlled by pH and redox conditions, precipitation-dissolution, sorption-desorption, and polymerization reactions (Baes and Mesmer, 1976; Cruywagen, 1999; Wanty and Goldhaber, 1992; Wehrli and Stumm, 1988). While V can exist in a range of oxidation states from V(–I) to V(V), the most common in terrestrial waters are V(V), V(IV), and V(III) (Baes and Mesmer, 1976; Wanty and Goldhaber, 1992). Redox conditions are a strong control on V mobility in the environment (Figure 2.1). Aqueous V speciation in oxic waters is dominated by the mobile V(V) oxyanions $H_2VO_4^-$, HVO_4^{2-}, and VO_4^{3-} ($H_3VO_4^0$ is negligible) from pH 4 to 14, while the V(V) oxycation VO_2^+ dominates at low pH (Baes and Mesmer, 1976; Wehrli and Stumm, 1989). Through abiotic and biotic V(V) reduction, aqueous V(IV) (i.e., VO^{2+}, $VOOH^+$, $VO(OH)_2^0$, $VO(OH)_3^-$) and V(III) (i.e., V^{3+}, VOH^{2+}, $V(OH)_2^+$, $V_2(OH)_2^{4+}$) species can persist under anoxic conditions and sorb to minerals surfaces or readily hydrolyze and precipitate as (hydr)oxides (Figure 2.1) (Baes and Mesmer, 1976; Carpentier et al., 2003; Chen and Liu, 2017; Ortiz-bernad et al., 2004; Wanty and Goldhaber, 1992).

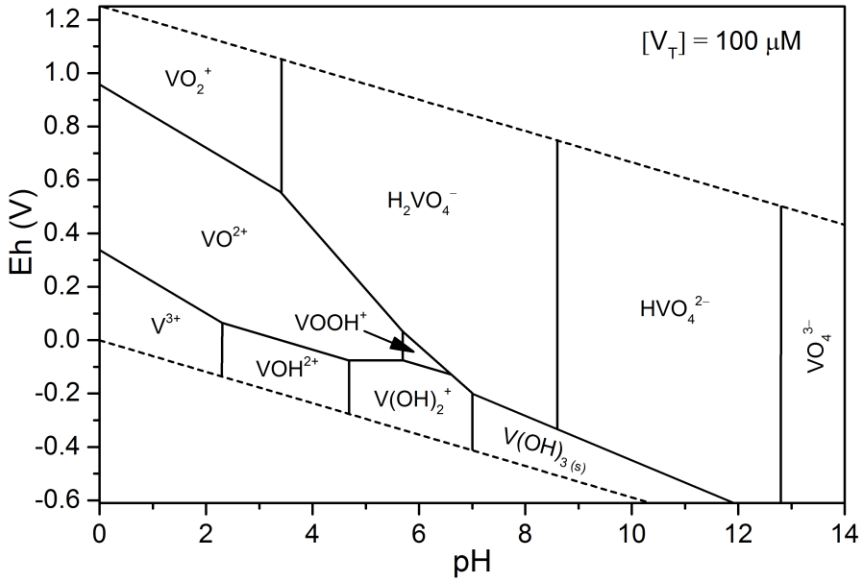

Figure 2.1. Eh – pH diagram for soluble and insoluble V species at 100 µM.

Complexation with inorganic and organic ligands strongly influences V mobility in aqueous systems and affects its sorption to mineral interfaces. Thermodynamic constants for various aqueous complexation reactions that affect V mobility have been reported (Baes and Mesmer, 1976; Chen and Liu, 2017; Cruywagen, 1999; Wanty and Goldhaber, 1992; Wehrli and Stumm, 1989). Briefly, V(V) dominates in oxic conditions as $[H_xVO_4]^{(3-x)-}$ or VO_2^+ under more acidic conditions and forms only a few weak complexes with organic matter, which may impede its reduction to V(IV) and V(III). Conversely, V(IV) complexes more readily with organic and inorganic ligands, and forms strong aqueous complexes as $VOSO_4^0$, $VOCl^+$, and $VOCO_3^0$. Organic complexes can also stabilize the vanadyl cations and prevent oxidation to V(V) (Reijonen et al., 2016; Wanty and Goldhaber, 1992; Wehrli and Stumm, 1989, 1988). Due to limited thermodynamic data for V(III) few aqueous complexes are known to form; however, chloride (VCl^{2+}) and sulfate (VSO_4^+) complexes have been observed (Wanty and Goldhaber, 1992). At elevated V concentrations (> 250 µg L^{-1}), polymerization and condensation of aqueous vanadate produces dimers ($[H_xV_2O_7]^{(4-x\ -)}$), trimers ($V_3O_{10}^{5-}$), tetramers ($V_4O_{12}^{4-}$), pentamers ($V_5O_{15}^{5-}$), hexamers ($V_6O_{18}^{6-}$), and decamers ($[H_xV_{10}O_{28}]^{(6-x)-}$) between pH 2 and 10 (Figure 2.2). Additionally, precipitation of V(IV) and V(III) (hydr)oxides at low temperature (i.e., < 100 °C), predominantly as $VO(OH)_{2(s)}$ and $V(OH)_{3(s)}$, can limit dissolved V concentrations. Natural and synthetic V oxides, such as vanadium pentoxide [V_2O_5], vanadium tetroxide [V_2O_4], vanadium dioxide [VO_2], and vanadium trioxide [V_2O_3] are kinetically limited at low temperatures and

crystalize at temperatures exceeding 300 °C (Cook, 1947). Vanadium oxides have a wide array of applications spanning from industrial processes during steel manufacturing (i.e., ferrovanadium), pigments, catalysts, and battery manufacturing; however, V oxide dissolution is a significant source of vanadium release (Hu et al., 2018; Huang et al., 2015).

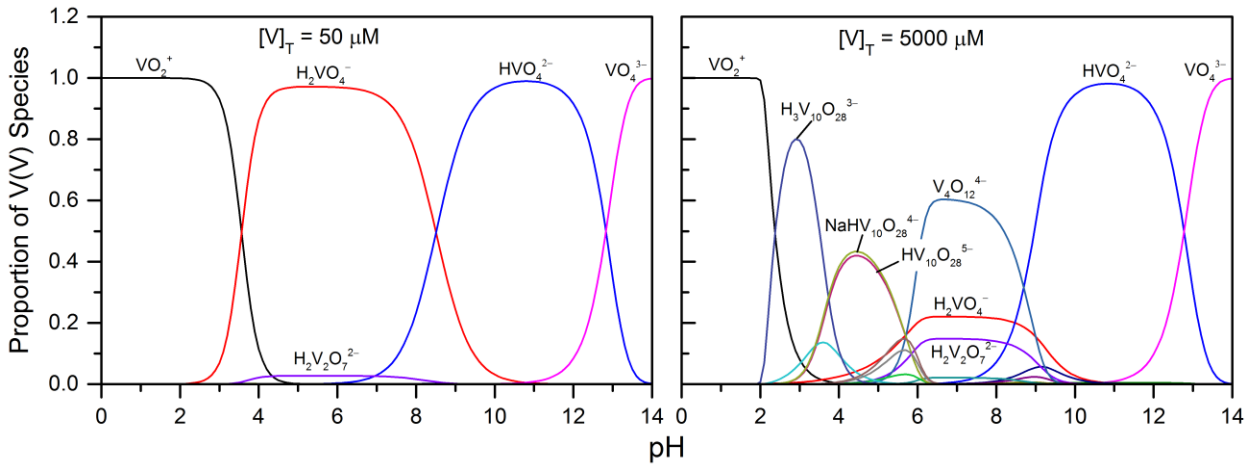

Figure 2.2. V(V) speciation diagram at 50 (left) and 5000 µM (right).

Vanadium reduction can be catalyzed by Fe(II) bearing minerals, reduced sulfur, microbes, and soil organic matter. Reduction of aqueous VO_2^+ and $H_2VO_4^-$ (Eq. 2.1) in the presence of magnetite and ilmenite is rapid at pH 3 and limited at 5 and 7 (White and Peterson, 1996). Similarly, thermodynamic data and experimental work collected by Wanty and Goldhaber (1992) demonstrated V(IV) reduction to V(III) by S(−II) can occur in sulfidic environments (Eqs. 2.2, 2.3). *Shewanella putrefaciens*, *Geobacter metallireducens*, *Shewanella oneidensis*, and *Pseudomonas* strains can actively respire V using V(V)/V(IV)/V(III) redox couples (Carpentier et al., 2003; Crans et al., 2004; Ortiz-bernad et al., 2004; Li and Le, 2007). The V(V)/V(IV) redox couple has been suggested to be more energetically favourable than common Fe(III) electron acceptors making *in situ* microbial remediation a suitable strategy for dissolved V removal at contaminated sites (Carpentier et al., 2003). Both biotic and abiotic reduction can decrease bioavailable V(V) through subsequent V hydroxide precipitation and sorption reactions.

$$3[Fe^{2+}]_{oxide} + 4H^+ + 2VO_2^+ \leftrightarrow 2[Fe^{2+}]_{oxide} + 2VO^{2+} + Fe^{2+} + 2H_2O \quad (2.1)$$

$$VO(OH)^+ + \frac{1}{2}H_2S \leftrightarrow V(OH)_2^+ + \frac{1}{2}S^0 \quad (2.2)$$

$$VO(OH)^+ + \frac{1}{2}HS^- \leftrightarrow V(OH)_2^+ + \frac{1}{2}S^0 \quad (2.3)$$

2.4. Vanadium Attenuation

Complexation reactions with mineral surfaces is a major control on V mobility in terrestrial and marine waters (Bennett et al., 2018; Gustafsson, 2019; Huang et al., 2015; Hudson-Edwards et al., 2019; Nesbitt, 2016; Wright and Belitz, 2010). Similar to other oxyanion-forming metal(loid)s, V adsorption is dependent on aqueous $[V]_T$, ionic strength, pH, redox conditions, and competing ions (Borch et al., 2010; Gustafsson, 2019; Huang et al., 2015; Shaheen et al., 2019). Vanadium adsorption has been reported for δ-Al_2O_3, anatase [TiO_2], goethite [α-FeOOH], ferrihydrite, Fe(III)/Cr(III) hydroxide, kaolinite, and montmorillonite (Brinza et al., 2019, 2008; Larsson et al., 2017; Motschi and Rudin, 1984; Naeem et al., 2007; Peacock and Sherman, 2004; Prathap and Namasivayam, 2010; Wehrli and Stumm, 1989, 1988; Zhu et al., 2018). Analogous to phosphate and other oxyanions, V undergoes ligand exchange despite expected electrostatic repulsion (Sigg and Stumm, 1980), and readily adsorbs to mineral surfaces from pH 3 to 8 (Brinza et al., 2008; Peacock and Sherman, 2004; Prathap and Namasivayam, 2010; Wehrli and Stumm, 1989). Sorption of $H_2VO_4^{2-}$ and VO^{2+} onto δ-Al_2O_3 and TiO_2 results in the formation of inner sphere monodentate and bidentate complexes at >AlOH and >TiOH Lewis acid sites (Motschi and Rudin, 1984; Wehrli and Stumm, 1989). Recent studies utilizing extended X-ray absorption fine structure spectroscopy (EXAFS) have identified edge- and corner-sharing complexes during vanadate adsorption onto ferrihydrite and goethite surfaces, respectively (Larsson et al., 2017; Peacock and Sherman, 2004). Differences in vanadate adsorption complexes at ferrihydrite and goethite surfaces is thought to be related to variations in crystallinity. Edge-sharing complexes at ferrihydrite surfaces are likely caused by the higher abundance of available singly coordinated hydroxyl groups at Fe(III) octahedral sites, compared to the more crystalline structure of goethite. Competition for sorption sites with other dissolved ions, including arsenate, selenate, molybdate, and phosphate may also affect V sorption (Blackmore et al., 1996; Brinza et al., 2008; Jeong et al., 2007; Prathap and Namasivayam, 2010). For example, when in solution together vanadate and phosphate compete for surface sites in approximately equal proportions (PO_4: 55%; VO_4: 45%) onto ferrihydrite surfaces (Blackmore et al., 1996; Brinza et al., 2008; Larsson et al., 2017).

2.5. Iron Minerals in Soils and Sediments

Iron-bearing minerals are ubiquitous near Earth' surface and play a fundamental role in biogeochemical cycling of trace metals, nutrients and contaminants (Borch et al., 2010). Iron(III)

minerals including ferrihydrite, goethite, and hematite are prevalent in oxic soils and sediments, where they may occur as weathering products of parent rock material, colloid materials, or secondary coatings on detrital minerals (Cornell and Schwertmann, 2003). Likewise, Fe(II) minerals including pyrite, mackinawite, siderite and magnetite have significant roles in contaminant and nutrient mobility within estuarine, near-shore, deep marine, stratified lakes, and groundwater systems where anoxic conditions persist (Johnston et al., 2014; Morse and Cornwell, 1987; Phillips et al., 2003; Rickard and Luther, 2007; Spadini et al., 2003; Wang et al., 2018). Numerous geochemical studies have focussed on sorption of contaminants (e.g., As, Se, and Cr) to Fe(III) (hydr)oxides (e.g., Dixit and Hering, 2003; Das et al., 2013). While Fe(II) sulfides, Fe(II) carbonate (i.e., siderite), green rust [$Fe^{II}_4Fe^{III}_2(OH)_{12}(CO_3^{2-},SO_4^{2-})$] and magnetite have received more attention recently (e.g., Farquhar et al., 2002; Jönsson and Sherman, 2008; Scheinost and Charlet, 2008; Mitchell et al., 2013; Ma et al., 2014). White and Peterson (1996) described aqueous V(V) reduction to V(IV) in the presence of natural magnetite and ilmenite, yet V adsorption mechanisms and reduction pathways during interaction with Fe(II)-bearing phases have yet to be described in detail.

CHAPTER 3: AQUEOUS VANADATE REMOVAL BY IRON(II)-BEARING PHASES UNDER ANOXIC CONDITIONS

3.1. Abstract

Vanadium contamination is a growing environmental hazard worldwide. Aqueous vanadate ($H_xV^VO_4^{(3-x)-}{}_{(aq)}$) concentrations are often controlled by surface complexation with metal (oxyhydr)oxides in oxic environments. However, the geochemical behaviour of this toxic redox-sensitive oxyanion in anoxic environments is poorly constrained. Here I describe results of batch experiments to determine kinetics and mechanisms of aqueous $H_2V^VO_4^-$ (100 μM) removal under anoxic conditions in suspensions (2 g L^{-1}) of magnetite, siderite, pyrite, and mackinawite. Parallel experiments using ferrihydrite (2 g L^{-1}) and $Fe^{2+}{}_{(aq)}$ (200 μM) are also presented for comparison. Siderite and mackinawite removed ≥ 90 % of aqueous vanadate after 3 h and kinetic rates were generally consistent with ferrihydrite. Magnetite removed ~50% of aqueous vanadate after 48 h, whereas removal was limited for pyrite. Uptake by $Fe^{2+}{}_{(aq)}$ was observed after 8 h, concomitant with precipitation of secondary Fe phases. X-ray absorption spectroscopy revealed V(V) reduction to V(IV) and formation of bidentate corner-sharing surface complexes on magnetite and siderite, and with $Fe^{2+}{}_{(aq)}$ reaction products. These data also suggest that V(IV) and V(III) is incorporated into the mackinawite structure. Overall, I demonstrated that Fe(II)-bearing phases can promote aqueous vanadate attenuation and, therefore, limit dissolved V concentrations in anoxic environments.

3.2. Introduction

Vanadium contamination of terrestrial and aquatic ecosystems is a growing environmental hazard due to increased releases from mining, steel making, energy production, and other anthropogenic activities (Gustafsson, 2019; Huang et al., 2015; Schlesinger et al., 2017; Watt et al., 2018). Dissolved V concentrations typically range from 0.5 to 2.4 μg L^{-1} in surface waters due to natural weathering of geologic materials. Elevated aqueous concentrations may result from leaching of V-enriched waste materials, including steel slag and mine wastes generated at coal, bauxite, uranium, phosphate and oil sands operations (Hobson et al., 2018; Huang et al., 2015;

Hudson-Edwards et al., 2019; Mayes et al., 2011; Nesbitt and Lindsay, 2017; Schlesinger et al., 2017; Shiller and Boyle, 1987; Yang et al., 2014). At higher concentrations, vanadate oxyanions ($H_xV^VO_4^{(3-x)-}{}_{(aq)}$) can be acutely toxic to aquatic organisms (Puttaswamy et al., 2010; Puttaswamy and Liber, 2011), bacteria (Larsson et al., 2013), and humans (Rehder, 1991; Seargeant and Stinson, 1979; Yu and Yang, 2019) due to similarities with phosphate inhibiting Ca-, Na- and K-ATPase ion pumps and cellular uptake through ion mimicry. Despite its inclusion on the USEPA contaminant candidate list, few jurisdictions have established soil or water quality guidelines for V (Environment and Climate Change Canada, 2016; RIVM Letter Report 601714021/2012; National Institute for Public Health and the Environment, 2012; USEPA, 2016). Recent research has presented a hazardous concentration endangering 5% of species (HC5) to be 50 μg L^{-1} for freshwater aquatic organisms (Schiffer and Liber, 2017). Canada established a criterion for V in soil of 130 mg kg^{-1} and recently instituted water quality guidelines of 120 μg L^{-1} and 5 μg L^{-1} for freshwater and marine waters, respectively (Canadian Council of Ministers of the Environment, 1999; Environment and Climate Change Canada, 2016).

Aqueous V speciation is highly dependent on $[V]_T$, pH, and redox conditions, which strongly affect surface complexation and the solubility of discrete V phases. While V exists in a range of oxidation states from V(−I) to V(V), the most prevalent in near-surface environments are V(V), V(IV), and V(III) (Gustafsson, 2019; Huang et al., 2015; Shaheen et al., 2019). Under oxic conditions, $H_2V^VO_4^-{}_{(aq)}$ is the predominant species at circum-neutral pH, while VO_2^+ dominates under acidic (i.e., pH < 3) conditions. Reduction of V(V) to V(IV) or V(III) can limit solubility through precipitation of V (hydr)oxides or enhanced sorption at mineral surfaces (Nesbitt and Lindsay, 2017; Ortiz-bernad et al., 2004; Wanty and Goldhaber, 1992; White and Peterson, 1996). Vanadium(V) reduction to V(IV) leads to the formation of aqueous vanadyl species VO^{2+}, $VOOH^+$, and $VO(OH)_3^-$, and further reduction produces aqueous V(III) as V^{+3}, VOH^{2+}, and $V(OH)_2^+$ (Baes and Mesmer, 1976; Chen and Liu, 2017; Wehrli and Stumm, 1989). Removal of aqueous V(V) or V(IV) by reduction to V(IV) and V(III) has been observed in laboratory and field settings through reaction with $H_2S_{(aq)}$, Fe(II)-oxide surfaces, organic compounds, and anaerobic microbial respiration (Carpentier et al., 2003; Ortiz-bernad et al., 2004; Reijonen et al., 2016; Wanty and Goldhaber, 1992; White and Peterson, 1996).

Biogeochemical cycling of C, S, Fe and Mn can strongly affect contaminant mobility in the environment (Borch et al., 2010). In particular, Fe (oxyhydr)oxides and Fe sulfides in natural soils,

sediments, and aquifers play a key role in the sequestration of organic and inorganic contaminants (Cornell and Schwertmann, 2003; Rickard and Luther, 2007). Previous studies have established how surface reactions and redox processes affect the environmental mobility of oxyanion forming metal(loid)s (e.g., As, Se, and Cr) with Fe (oxyhydr)oxides (e.g., Dixit and Hering, 2003; Myneni et al., 1997) and Fe sulfide minerals (e.g., Couture et al., 2013; Han et al., 2011). In comparison, aqueous V reactions have received less attention with the current literature being limited to sorption onto metal (oxyhydr)oxides (Brinza et al., 2019; Larsson et al., 2017; Naeem et al., 2007; Peacock and Sherman, 2004; Wehrli and Stumm, 1989) and clay minerals (Wisawapipat and Kretzschmar, 2017; Zhu et al., 2018) under oxic conditions. Wehrli and Stumm (1989) showed the adsorption of V(V) onto TiO_2 and δ-Al_2O_3 surfaces with the formation of inner-sphere monodentate complexes at low pH (< 3) as $V^VO_2^+$, while at higher pH (i.e., 4 to 8) $H_2V^VO_4^-{}_{(aq)}$ sorption occurred *via* inner sphere complexes similar to phosphate. These authors also found that $V^{IV}O^{2+}{}_{(aq)}$ removal by TiO_2 and δ-Al_2O_3 results from formation of bidentate surface complexes. Recent EXAFS studies demonstrated that $H_2V^VO_4^-{}_{(aq)}$ uptake by 2-line ferrihydrite (Brinza et al., 2019; Larsson et al., 2017) and goethite (Peacock and Sherman, 2004) at circum-neutral pH occurs via formation of inner-sphere edge and corner-sharing surface complexes, respectively. Under anoxic conditions, White and Peterson (1996) found enhanced reduction of vanadate in the presence of magnetite and ilmenite at pH 3 related to dissolved aqueous Fe^{2+}, whereas at pH 5 and 7 these authors observed decreased aqueous V(V) reduction and limited removal, as a result of increased sorption at magnetite and ilmenite surfaces. However, detailed kinetic and spectroscopic analysis of V(V) removal by Fe(II)-phases has not been constrained. Therefore, investigating redox processes involving interactions between V and Fe(II)-bearing mineral surfaces under anoxic conditions will improve understanding of environmental V geochemistry.

Here I describe results of batch experiments and associated analyses to examine rates and mechanisms of aqueous $H_2V^VO_4^-{}_{(aq)}$ removal under anoxic conditions by magnetite [Fe_3O_4], pyrite [FeS_2], mackinawite [FeS], and siderite [$FeCO_3$]. These results are compared to parallel experiments with 2-line ferrihydrite [$5Fe_2O_3{\cdot}9H_2O$], as well as reaction with aqueous Fe^{2+}. Aqueous concentrations were measured using inductively coupled plasma–mass spectrometry (ICP–MS). Solid-phase V associations were examined by transmission electron microscopy–energy dispersive X-ray spectroscopy (TEM–EDX), X-ray absorption spectroscopy near edge structure (XANES) spectroscopy, and extended X-ray absorption fine structure (EXAFS)

spectroscopy. Prevalent reducing conditions are known to limit V mobility within aquifers (Wright et al., 2014), contaminated sites (Nesbitt and Lindsay, 2017), and marine systems (Bennett et al., 2018); however, molecular mechanisms involved during V removal by Fe(II)-phases remains poorly constrained. Results improve understanding of V mobility in anoxic conditions and provides new insight into environmental V geochemistry.

3.3. Materials and Methods

Batch experiments and all associated sample preparation occurred under an anoxic atmosphere ($\leq$ 5% H_2, balance N_2) in an anaerobic chamber (Coy Laboratory Products, USA). All solutions were prepared using ultra-pure water (18.2 MΩ cm^{-1} resistivity) that was first purged with $N_{2(g)}$ for at least 24 h. Prior to use, all glassware and the polytetrafluoroethylene (PTFE) paddle mixers were soaked for 24 h in 10% (v/v) oxalic acid, then soaked for 24 h in 10% (v/v) HCl, and rinsed thoroughly with deionized (DI) water.

3.3.1. Experimental Solids

Ferrihydrite, siderite, mackinawite, and $V^{IV}O(OH)_{2(s)}$ were synthesized using modified versions of methods described by Cornell and Schwertmann (2003), Qu et al. (2011), Wolthers et al. (2003), and Chen et al. (2018), respectively (Supporting Information A.1). Commercially-available magnetite (<5 nm, 95% purity; Sigma-Aldrich, USA) and pyrite (<44 nm, 99.8% purity; Sigma-Aldrich, USA) was washed in 10 % (v/v) HCl and 0.001M HCl, respectively, and then rinsed with $N_{2(g)}$-purged ultra-pure water and freeze dried. The mineralogy of synthesized and purchased solids was confirmed by powder X-ray diffraction (XRD) and Raman spectroscopy (Supporting Information). Particle size was estimated from TEM images and specific surface area (SSA) was determined using the Brunauer-Emmett-Teller N_2 sorption method (Table A.1).

3.3.2. Batch Experiments

Batch experiments were conducted in the anaerobic chamber using 2000 mL glass beakers. The final background electrolyte solution was 0.05 M NaCl and 0.005 M MOPS adjusted to pH 7.0 ± 0.1. The MOPS buffer was chosen based on previous studies showing it does not significantly affect oxyanion sorption between pH 6 and 8.5 (Bostick and Fendorf, 2003; Couture et al., 2013; Wolthers et al., 2005b). A vanadate stock solution was prepared by dissolving 13.9 mg of $Na_3V^VO_4$ (99.98%, Sigma-Aldrich, USA) into 500 mL of ultra-pure water. Mineral suspensions were prepared by adding 2.0 g of a given phase to a separate 500 mL of background electrolyte. For

reactions involving $Fe^{2+}_{(aq)}$, solutions were prepared by dissolving 25.4 mg of $FeCl_2$ (> 98.0 %, Sigma-Aldrich, USA), with no mineral phase present, into 500 mL of the background electrolyte solution. Prior to initiating the experiments, the 500 mL mineral suspensions or $Fe^{2+}_{(aq)}$ solution were stirred continuously with an overhead mixer (RW 20 digital, IKA Works, Inc., USA) fitted with a PTFE paddle. After 3 h of equilibration, 500 mL of the aqueous vanadate solution was quickly added, bringing the total volume to 1000 mL. This method produced initial V concentration of 100 µM (5.0 mg L^{-1}), which is relevant to mining-impacted sites yet low enough to limit formation of polynuclear V species (Hobson et al., 2018; Hudson-Edwards et al., 2019; Mayes et al., 2011; Nesbitt and Lindsay, 2017). Over the course of the experiment redox potential (Eh) and pH were monitored continuously so that pH remained at 7.0 ± 0.1 and were adjusted as needed at late time during the 48 h experiments using 0.1 M HCl and NaOH.

Two different experimental durations were used (3 h, 48 h) to obtain high-resolution aqueous-phase data for kinetic modeling and solid-phase samples for examining V removal mechanisms. Samples were collected from triplicate 3 h experiments at the following times: 0, 0.5, 1.0, 1.5, 2.0, 2.5, 3.0, 3.5, 4.0, 4.5, 5.0, 10, 20, 30, 40, 60, 120, 180 min (n = 19). Samples were collected from the 48 h experiment at the following times: 0, 1.0, 2.5, 5.0, 10, 20, 30, 40, 60, 120, 180, 240, 480, 1080, 1440, and 2880 min (n = 16). Each 4 mL sample was collected into an all-plastic syringe (Norm-Ject, HSW GmbH, Germany) and passed through a sterile 0.1 µm polyethersulfone syringe filter membrane (Minisart, Sartorius AG, Germay) into high-density polyethylene bottles (Nalge Nunc International Corp., USA). Samples for ICP-MS (Nexion 300D, Perkin Elmer, Inc., USA) analysis were acidified to pH < 2 with 25 µL of trace-metal grade HNO_3 acid (OmniTrace, Millipore Sigma, USA). Following the final sample time, each experiment was terminated by vacuum filtering remaining solution through 8 µm cellulose filter paper (Whatman Grade 2, GE Healthcare, USA). Retained solids were transferred into 2 mL cryogenic polypropylene tubes, flash frozen in liquid nitrogen and stored cryogenically (i.e., ~80 K) until analysis. Sample names referenced herein correspond to experiment termination times (3 and 48 h) and reaction phase used, including ferrihydrite (3-Fh and 48-Fh), magnetite (3-Mag and 48-Mag), siderite (3-Sd and 48-Sd), mackinawite (3-Mck and 48-Mck), pyrite (3-Py and 48-Py), and aqueous Fe^{2+} (3-Fe^{2+} and 48-Fe^{2+}).

3.3.3. X-ray Absorption Spectroscopy

Synchrotron based powder X-ray absorption spectroscopy was performed at the Canadian Light Source (CLS) on beamline 06-B1-1 (SXRMB). Solid-phase samples from each batch were thawed and dried overnight in a vacuum desiccator within the anaerobic chamber. These samples were homogenized using an agate mortar and pestle, and approximately 0.05 g of each sample was mounted to a conductive Cu plate using two-sided adhesive C tape. Several reference materials including sodium orthovanadate [$Na_3V^VO_4$], vanadyl hydroxide [$V^{IV}O(OH)_2$], vanadyl sulfate [$V^{IV}OSO_4$] (≥ 99.99 %, Sigma Aldrich, Inc., USA), and V(III) chloride [$V^{III}Cl_3$] (> 99%, Sigma Aldrich, Inc., USA) were also prepared for analysis. The samples were sealed in a vacuum desiccator under an anoxic atmosphere for transport to the CLS (< 15 min).

The Cu plates were quickly transferred from the vacuum desiccator to the solid state end station, which was operated at high vacuum ($10^{-8.7}$ Torr) and ambient temperature during collection of fluorescence spectra with a 7-element Si drift detector (RaySpec Ltd., UK). Incident X-ray energy was selected using a monochromator fitted with paired Si(111) crystals and the beam spot size was focussed to 1 mm (vertical) by 4 mm (horizontal). Replicate V K-edge spectra were obtained for samples (n = 3) and reference materials (n = 3) by scanning incident energy from 100 eV below the theoretical absorption edge (5465 eV) to k = 14 $Å^{-1}$ at steps of 0.25 eV in the XANES region and 0.05 $Å^{-1}$ in the EXAFS region.

Data processing and analysis was performed using Athena software (Version 0.9.26), which is a component of the Demeter software package (Ravel and Newville, 2005). Data reduction, energy calibration, pre-edge background subtraction, post-edge normalization, and background removal were performed prior to EXAFS modeling. Non-linear least squares fitting of EXAFS data were performed using ARTEMIS by generating amplitude and phase functions with FEFF 6.0 for all reference V compounds, and a modified $Na_3V^VO_4$ and $V^{IV}OSO_4$ structure with Fe(III) substitution. Pseudo-radial distribution functions were obtained through Fourier transform of $\chi(k)\cdot k^3$ functions over varying k-ranges depending on data quality. Due to crystal glitchs above ~10.5 $Å^{-1}$, all EXAFS models were constrained between 2.5 and 10.5 $Å^{-1}$.

3.3.4. Microscopy

A TEM-EDX (HT7700, Hitachi High-Technologies Corp., Japan) were used to examine crystallite size and morphology of reacted solid-phase samples. The samples were prepared for

mounting in the anaerobic chamber following procedures used for XAS measurements. Samples prepared for TEM-EDX (Hitachi HT7700) were suspended in 100% ethanol and dispersed onto C-coated Cu grids and allowed to dry in the glovebox until analysis. During imaging, the TEM operated at an accelerating voltage of 120 kV.

3.3.5. Kinetic Reaction Modeling

Rate constants were initially determined by fitting first, pseudo first, and second order models to aqueous concentration data averaged for replicate batches (Figure A.1). However, similar to other oxyanion-forming elements (e.g., As), V removal may proceed through multiple reaction pathways including adsorptive equilibrium, incorporation into mineral structures, and reduction. Therefore, a mixed-reaction modeling approach for V removal that integrates (i) fast, reversible uptake via outer sphere complexation represented by K_{eq}, (ii) slow, rate-controlled reversible uptake, corresponding to diffusion of vanadate to sorption sites or formation of inner-sphere complexation represented by rate constants k_f (adsorption) and k_b (desorption), and (iii) slow, irreversible uptake by intra- or interparticle diffusion or the formation of surface precipitates represented by k_i (Couture et al., 2013; Zhang and Selim, 2005). Both the initial kinetic (Table A.2) and mixed-reaction model (Table 3.1) parameters were fit to the 3 h and 48 h kinetic batch experiment data by inverse modeling to minimize the root-mean-square error (RMSE).

3.4. Results and Discussion

3.4.1. Vanadate Removal Kinetics

Similar to other metal(loid) oxyanions, $H_2V^VO_4^-$ sorption onto ferrihydrite (3-Fh, 48-Fh) is a fast process reaching 90% removal (46 µmol g^{-1}) by 40 min and complete removal (46 µmol g^{-1}) after 3 h (Figure 3.1a). These results agree with previous experiments performed at pH 7.0, which reported $H_2V^VO_4^-$ adsorption *via* ligand exchange at Fe(III) (oxyhydr)oxide surfaces (Brinza et al., 2019; Larsson et al., 2017; Peacock and Sherman, 2004). In comparison, $H_2V^VO_4^-$ uptake by magnetite (3-Mag, 48-Mag) plateaued within 10 min at 14 µmol g^{-1} (~32% removal) and increased to 18 µmol g^{-1} (52% removal) after 48 hr (Figure 3.1a). White and Peterson (1996) observed limited capacity for $H_2V^VO_4^-$ reduction by natural magnetite samples at pH 7.0, therefore, removal of V(V) at pH 7 can be attributed to adsorption at magnetite.

Vanadate removal by siderite varied slightly due to variations in crystallite size and, therefore, surface area (Table A.1). Uptake of $H_2V^VO_4^-$ by siderite (3-Sd-avg, 48-Sd) reached

42 μmol g^{-1} (90% removal) after 3 h and increased to 46 μmol g^{-1} (~100% removal) following 48 h (Figure 3.1b). Aqueous Fe concentrations decreased from 114 to 94 μM over the first 4 h, and subsequently increased to 620 μM after 48 h (Figure A.2). The V removal rate and capacity for siderite correlated to SSA, where above 10 m^2 g^{-1} (3-Sd-b, 3-Sd-c, 3-Sd-d) kinetic rates are similar with an average K_{eq} value of 0.63, compared to 3-Sd-a (5.8 m^2 g^{-1}) with a K_{eq} of 0.30 (Table 3.1).

Table 3.1. Initial ($[V]_0$) and final ($[V]_f$) aqueous V concentrations along with estimated equilibrium constant (K_{eq}), rate constants, forward (k_f), backward (k_b), and irreversible (k_i), and goodness of fit parameters, R^2 and RMSE, obtained from multi-reaction modeling. Sample names correspond to experiment duration and mineral abbreviations including ferrihydrite (Fh), magnetite (Mag), mackinawite (Mck), and siderite (Sd).

Sample	Time (hr)	$[V]_0$ (μM)	$[V]_f$ (μM)	log K_{eq}	k_f (h^{-1})	k_b (h^{-1})	k_i (h^{-1})	R^2	RMSE
3-Fh	3	93.7	0.55	-0.2	29.2	17.3	0.01	0.997	1.60
48-Fh	48	90.2	0.08	-0.4	15.9	5.8	0.0007	0.998	0.64
3-Mag	3	92.1	61.5	-0.6	665.8	159.7	0.02	0.963	0.33
48-Mag	48	89.5	51.7	-0.4	525.8	189.5	0.003	0.90	0.57
3-Mck	3	91.1	0.13	0.4	69.1	178.2	0.03	0.985	0.44
48-Mck	48	89.9	0.0	0.5	28.0	79.7	0.00	0.972	0.64
3-Sd-a	3	87.0	31.2	-0.5	77.3	22.1	0.08	0.986	0.72
3-Sd-b	3	94.0	7.4	-0.2	118.1	81.8	0.05	0.994	0.64
3-Sd-c	3	92.1	13.6	-0.4	134.0	59.4	0.08	0.995	0.59
3-Sd-d	3	91.6	5.3	-0.1	115.5	86.9	0.06	0.991	0.69
3-Sd-avg	3	92.6	8.77	-0.2	121.3	75.4	0.06	0.995	0.58
48-Sd	48	92.7	0.04	-0.2	27.3	16.9	0.0007	0.997	0.64

Mackinawite is a highly reactive metastable Fe(II) sulfide phase with the potential for sorption and reduction of metal(loid)s (Mitchell et al., 2013; Scheinost and Charlet, 2008). Attenuation of $H_2V^VO_4^-$ by mackinawite (3-Mck, 48-Mck) was rapid and 100% removal (45 μmol g^{-1}) was observed after 1 h (Figure 3.1c). During the 48 h experiment aqueous Fe concentrations increased from 265 μM to 804 μM (Figure A.2). In contrast to mackinawite, $H_2V^VO_4^-$ removal by pyrite under the experimental conditions was limited (Figure 3.1d). This can be attributed to the low SSA of authigenic pyrite (Table A.1), and limited aqueous Fe^{+2} in solution

due to pyrite low solubility at circumneutral pH. Vanadium removal during reaction with aqueous Fe^{2+} (48-Fe^{2+}) was limited after 3 h, but increased to 22 µmol g^{-1} (47% removal) after 48 h (Figure 1d). This decrease in aqueous V concentrations corresponded to a decrease in aqueous Fe concentrations from 200 to 143 µM after 48 h (Figure A.2).

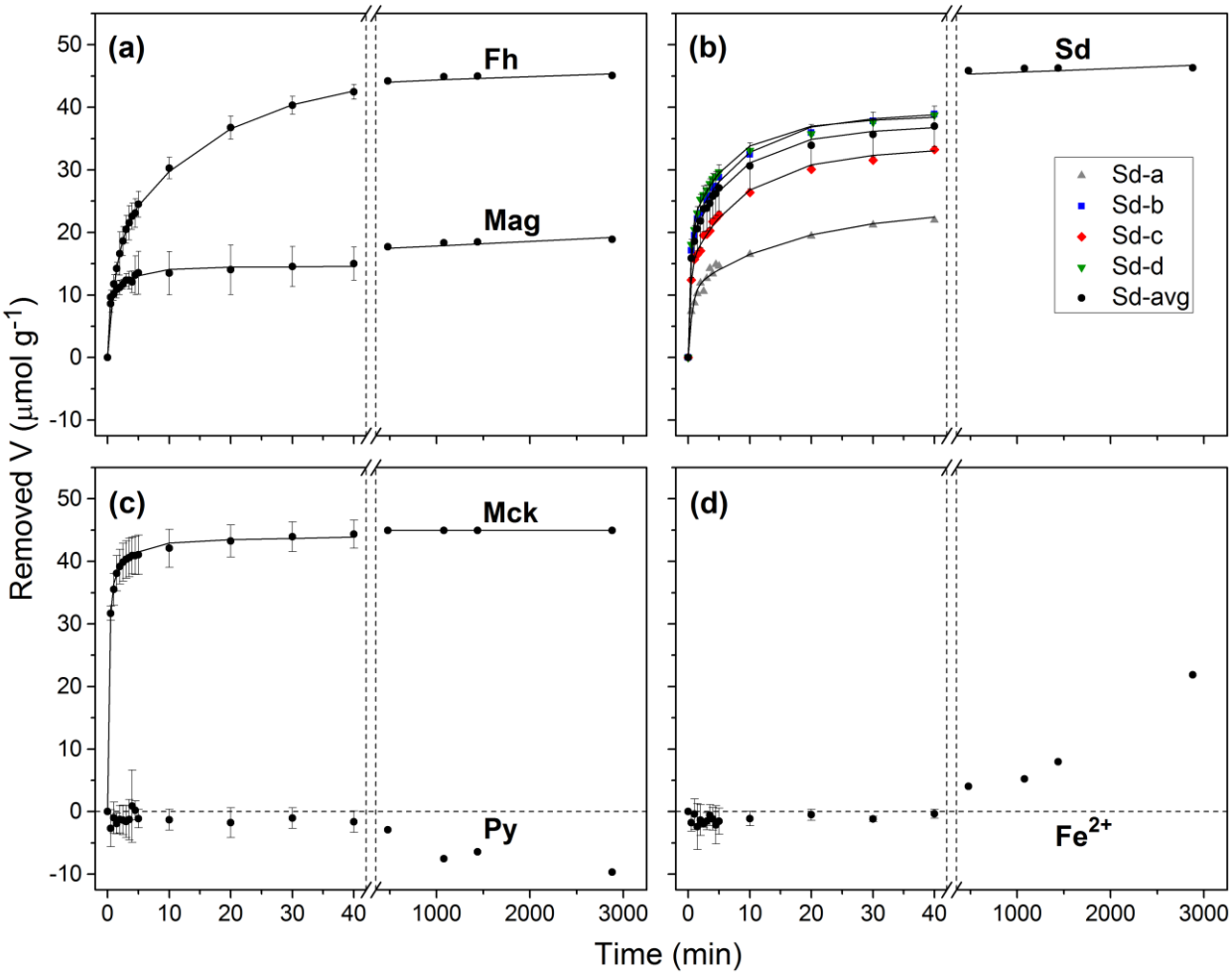

Figure 3.1. Measured (closed circles) and multi-reaction modeled (solid lines) concentrations of aqueous V during batch experiments with (a) ferrihydrite (Fh) and magnetite (Mag), (b) siderite (Sd), (c) mackinawite (Mck) and pyrite (Py), and (d) aqueous Fe^{2+}. Siderite kinetic experiments corresponding to Sd-a, Sd-b, Sd-c, and Sd-d (b) are plotted to demonstrate the effect of SSA on removal rates.

3.4.2. Spectroscopic Analyses

Vanadium oxidation states were assessed using V K-edge XANES collected for experimental samples and reference materials (Figure 3.2; Figure 3.3). Pre-edge intensity and energy position were compared to previously-reported values for $H_2V^{V}O_4^{-}{}_{(aq)}$ and $V^{IV}O^{2+}{}_{(aq)}$

(Larsson et al., 2017). Vanadium pre-edge peak height, energy position and area correlate to oxidation state and are sensitive to coordination changes (Bennett et al., 2018; Chaurand et al., 2007; Kaur et al., 2009; Levina et al., 2014). As expected, normalized pre-edge peak height and area decreased with oxidation state in the reference materials following the order: $Na_3V^VO_4$ > $VO^{IV}(OH)_2 \approx VO^{IV}SO_4 >> V^{III}Cl_3$ (Table A.3). Based on methods developed by Chaurand et al. (2007), Levina et al. (2014) and Bennett et al. (2018), V oxidation states were estimated using a linear regression ($R^2 = 0.981$) of the normalized pre-edge peak area (Figure 3.2a; Table A.3). Using this approach on reference spectra yielded averaged oxidation states of +5.09 ($Na_3V^VO_4$), +3.95 ($V^{IV}O(OH)_2$), +3.87 ($V^{IV}OSO_4$), and +3.09 ($V^{III}Cl_3$) for the reference materials.

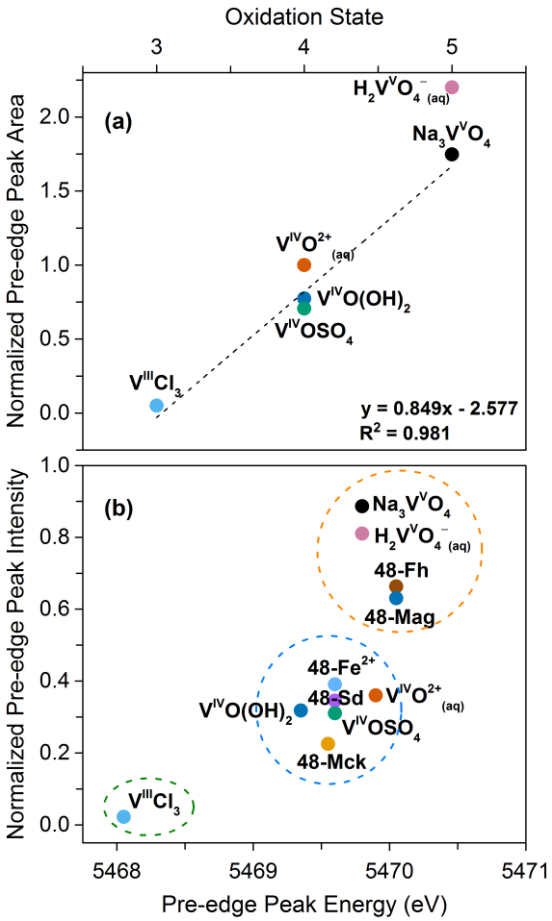

Figure 3.2. (a) Normalized pre-edge peak area and oxidation state with linear regression (dashed line) of V oxidation states in reference materials used to estimate average V oxidation state in experimental samples. (b) Normalized pre-edge peak intensity plotted against pre-edge energy position. Dashed circles indicate V(V) (orange), V(IV) (blue), and V(III) (green) oxidation states. Data for $H_2V^VO_4^-$ (aq) and $V^{IV}O^{2+}$(aq) from Larsson et al. (2017), these points were not included in the linear regression fit.

Vanadium associated with reacted ferrihydrite and magnetite samples are consistent with $Na_3V^VO_4$ spectra, which exhibits a smooth XANES feature and large normalized pre-edge peak (Figure 3.2b; Figure 3.3a), with an average oxidation of approximately +5. Spectra obtained for reacted siderite and aqueous Fe^{2+} displayed a slightly elevated edge region and dampened pre-edge peak height similar to $V^{IV}O(OH)_{2(s)}$, and $V^{IV}O^{2+}{}_{(aq)}$. Estimated oxidation states yielded +4.35 (3-Sd-a), +4.31 (3-Sd-b), +4.12 (48-Sd) and +4.29 (48-Fe^{2+}) indicating that sorbed V(IV) is the dominant oxidation state associated with reactions (Figure 3.2b). Similarly, V K-edge pre-edge peak height and area for mackinawite samples indicated oxidation states of +3.80 (3-Mck) and +3.64 (48-Mck), suggesting the presence of V(IV) and possibly minor amounts of V(III) (Table A.3). In addition, V in reacted mackinawite samples show a distinct XANES feature consistent with the $V^{IV}OSO_4$ reference (Figure 3.3).

Non-linear least squares modeling was performed for V K-edge EXAFS spectra of all references and experimental samples to determine bonding environments and assess vanadate removal mechanisms under anoxic conditions (Figure 3.3; Table A.4). Vanadium reference spectra were fit to tetrahedral ($Na_3V^VO_4$) and octahedral ($V^{IV}O(OH)_{2(s)}$, $V^{IV}OSO_4$, $V^{III}Cl_3$) coordination environments. The V(V) reference, $Na_3V^VO_4$, was consistent with previous fitting parameters (Brinza et al., 2019; Larsson et al., 2017). and exhibited a first shell V-O coordination number of 4 at 1.713 Å and a multiple scattering path around the VO_4 tetrahedron (3.14 Å). The $V^{IV}O(OH)_2$ reference was fit based on structural parameters from Krakowiak et al. (2012) and Besnardiere et al. (2016), where V(IV) is in a distorted octahedral coordination with the first shell V-O being a characteristic, singly coordinated short double bond (V=O) at 1.614 Å, followed by 4 coordinate *trans* V-O bonds at 2.000 Å, and an elongated V-O_{eq} bond at 2.527 Å. Long range photoelectron interactions in the $V^{IV}O(OH)_2$ structure were fit to 4 coordinate V-V backscatters at 3.04 Å, 3.24 Å, and 3.43 Å. Similarly, $V^{IV}OSO_4$ exhibits octahedral coordination with a single V=O bond, 4 coordinate V-O_{trans}, and singly coordinated V-O_{eq} at 1.597 Å, 2.018 Å, and 2.52 Å, respectively.(Cooper et al., 2003; Krakowiak et al., 2012) Following the V-O bonds, 2 coordinate V-S is fit at 3.27 Å, similar to $V^{IV}OPO_4$ structure (Wen et al., 2016). Lastly, $V^{III}Cl_3$ was fit with V-Cl, V-Cl_{trans}, and V-Cl_{eq} at 2.03 Å, 2.27 Å, and 2.41 Å, respectively, followed by repeating crystal structural units of 3 coordinate V-V backscatters at 3.41 Å and V-Cl backscatters at 4.80 Å in 6 coordination.

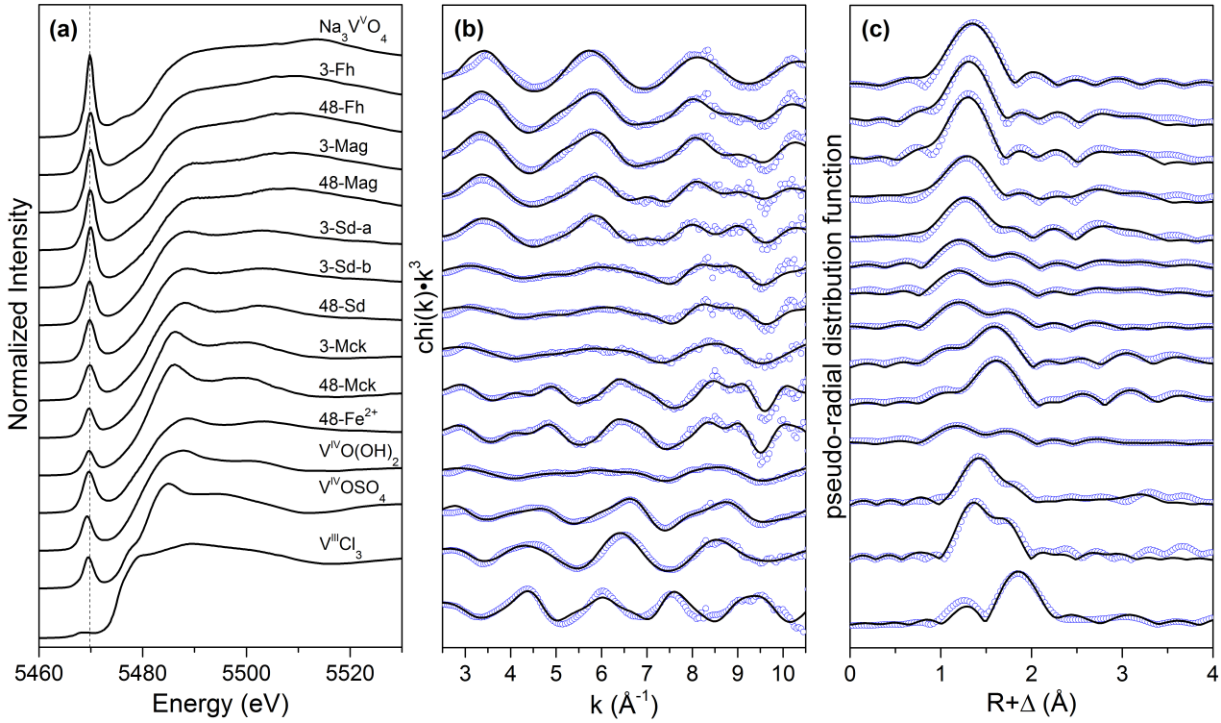

Figure 3.3. (a) Normalized absorbance of V K-edge XANES spectra for selected reference compounds and samples. Vertical dashed line indicates the theoretical V pre-edge peak position (5468.9 eV). (b) Measured (open circles) and modeled EXAFS (solid lines) k^3-weighted EXAFS spectra. (c) Pseudo-radial distribution functions for reference compounds and samples. Reference and sample spectra in panels (b) and (c) are ordered for consistency with panel (a).

Consistent with previous literature on vanadate sorption, bidentate complexes with tetrahedral V-O shell at 1.71 Å and a V^VO_4 tetrahedron multiple scattering path (3.17 Å) in 3 and 48 h ferrihydrite samples (3-Fh, 48-Fh) (Brinza et al., 2019; Larsson et al., 2017). A single Fe backscattering atom at 2.68 Å was fit similar to Larsson et al. (2017); however, I excluded the V-O-Fe multiple scattering path included by these authors. Rather, a second V-Fe scattering path was fit with a coordination number of 2.0, at 3.32 and 3.29 Å to 3-Fh and 48-Fh, respectively. The two V-Fe backscatters represent the concurrent formation of bidentate edge- and corner-sharing, which has previously been reported for other sorbed oxyanion forming metal(loid)s (e.g., As) on Fe (oxyhydr)oxide phases (Manceau, 1995). The addition of a bidentate corner-sharing complex could be a result of anoxic conditions or higher ionic strength background electrolyte used in this study (0.05 M NaCl) compared to Larsson et al. (2017). Vanadium removal by magnetite followed a similar mechanism to ferrihydrite and other oxyanion metal(loid)s (e.g., Jönsson and Sherman, 2008). A tetrahedral V-O shell was fit at 1.701 Å to the 3 h magnetite sample (3-Mag) with a V-Fe

scattering path (corner-sharing) at 3.33 Å with a coordination number of 2.0. A first shell tetrahedron at 1.701 Å indicates reduced V species were not present after 3 h of reaction time. In contrast, after 48 h (48-Mag) first shell V-O in 3.1 coordination at 1.673 Å suggests a mix of V(V) (as $V^{V}O_4$) and V(IV) (as $V^{IV}O^{2+}$). Fits were further improved by including a second V-O shell at an interatomic distance of 2.24 Å with a coordination of 2.1, which is consistent with bidentate $V^{IV}O^{2+}$ sorption. Similar to ferrihydrite fits, two V-Fe paths were fit at 2.65 and 3.31 Å indicative of bidentate edge- and corner-sharing complexation. While V-Fe edge-sharing distances for ferrihydrite (2.68 Å) and magnetite (2.65 Å) are significantly shorter than V-Fe backscattering path (2.78 Å) modeled by Larsson et al. (2017), edge-sharing distances presented here are consistent with *ab initio* calculations and modeling performed by Peacock and Sherman (2004).

Siderite is a highly reactive mineral that actively sorbs (Guo et al., 2013; Jönsson and Sherman, 2008) and reduces (Bibi et al., 2018; Scheinost and Charlet, 2008) trace metal(loid)s. Aqueous V removal by siderite (Figure 3.1b) suggests rates are dependent on surface area. Therefore, 3-Sd-a and 3-Sd-b V K-edge EXAFS spectra were separately modeled and compared to assess potential differences in removal mechanisms based on surface area. Secondary precipitates were apparent in the siderite (3-Sd, 48-Sd) and aqueous Fe^{2+} (48-Fe^{2+}) batch experiments attributed to $H_2V^{V}O_4^-$ reduction coupled with surficial or aqueous Fe^{2+} oxidation (Eqs. 3.1–3.3). Combined XRD and TEM-EDX results revealed minor amounts of mixed Fe^{2+}/Fe^{3+} green rust and Fe(III) (oxyhydr)oxide in the siderite (3-Sd, 48-Sid) and Fe^{2+} (48-Fe^{2+}) solids (Figure A.3). Needle-like morphologies consistent with lepidocrocite and goethite were noted in reacted siderite samples (3-Sd, 48-Sid), but were not apparent for precipitates from the Fe^{2+} experiment (48-Fe^{2+}). Vanadium co-precipitation, as $H_2V^{V}O_4^-$ or $V^{IV}O^{2+}$, with the secondary phases was not directly observed but was previously reported by Kaur et al. (2009) and Schwertmann and Pfab (1994).

Variations in EXAFS parameters for reacted siderite samples (3-Sd-a, 3-Sd-b, 48-Sd) were not apparent. First shell V-O was fit to interatomic distances of 1.660 Å, 1.651 Å, and 1.662 Å, with second shells (V-O) and third shells (V-Fe) consistent between the three samples (Table A.4). A second V-Fe scattering path was included for 3-Sd-a (3.66 Å) and 3-Sd-b (3.60 Å) with coordination numbers of ~1, which are indicative of monodentate sorption. This monodentate V-Fe complex was not apparent after 48 h, suggesting conversion to more energetically favorable bidentate corner-sharing complex. The formation of bidentate and monodentate surface complexes

simultaneously on metal (oxyhydr)oxide surfaces has been demonstrated to be thermodynamically favourable (Peacock and Sherman, 2004; Wehrli and Stumm, 1989). Similar to reacted siderite samples, aqueous Fe^{2+} reactions with vanadate produced precipitates with similar EXAFS parameters. Specifically, these precipitates exhibited a first shell V-O at 1.660 Å, followed by 2 O atoms at 1.955 Å and 2 coordinate Fe backscatters at 3.60 Å. Based on the Fe coordination and interatomic distances for the V-Fe backscatters (3.31 to 3.38 Å), the V K-edge EXAFS spectra indicate a bidentate corner-sharing complex forming on siderite, green rust, or Fe (oxyhydr)oxides consistent with previous studies of other oxyanion forming metal(loid)s (Farquhar et al., 2002; Guo et al., 2013; Jönsson and Sherman, 2008; Manning et al., 2002). First shell V-O distances for 3-Sd-a, 3-Sd-b, 48-Sd, and 48-Fe^{2+} are indicative of mixed sorbed V(V) and V(IV) species at approximately 25% and 75%, respectively. The presence of mixed V oxidation states helps explain the slightly elongate first shell V-O (1.651 - 1.662 Å) and larger than expected first shell coordination compared to the first shell of $V^{IV}O(OH)_2$ reference (1.614 Å).

$$H_2V^VO_4^-{}_{(aq)} + Fe^{2+}{}_{(aq)} + 3H^+ \leftrightarrow V^{IV}O(OH)^+{}_{(aq)} + Fe^{3+}{}_{(aq)} + 2H_2O \quad (3.1)$$

$$H_2V^VO_4^-{}_{(aq)} + Fe^{II}CO_{3(s)} + H_2O \rightarrow V^{IV}O(OH)^+{}_{(aq)} + Fe^{III}(OH)_{3(s)} + CO_3{}^{2-}{}_{(aq)} \quad (3.2)$$

$$H_2V^VO_4^-{}_{(aq)} + 6Fe^{2+}{}_{(aq)} + HCO_3{}^{2-}{}_{(aq)} + 12H_2O \rightarrow$$

$$V^{IV}O(OH)^+{}_{(aq)} + [Fe_4^{II}Fe_2^{III}(OH)_{12}][CO_3 \cdot 2H_2O]_{(s)} + 9H^+ \quad (3.3)$$

V K-edge spectra for reacted mackinawite (3-Mck, 48-Mck) samples revealed the presence of V(IV) and, possibly, V(III) incorporated into the tetragonal structure (Figures 3.2, 3.3). The incorporation of metal(loid)s *via* coprecipitation with mackinawite has been previously been demonstrated with metal cations (e.g., Ni^{2+}), selenium, (thio)arsenic, and technetium (Couture et al., 2013; Farquhar et al., 2002; Finck et al., 2012; Ikogou et al., 2017; Morse and Arakaki, 1993; Wilkin and Beak, 2017; Yalcintas et al., 2016). EXAFS fitting for V in reacted mackinawite samples were first attempted through $V^{IV}O^{2+}$ sorption and $V^{IV}O(OH)_2$ precipitation (octahedral coordination); however, χ^2_{red} and R factor goodness of fit parameters for 3-FeS and 48-FeS were optimized by fitting a single V=O bond at 1.57 and 1.58 Å, respectively, and S atoms with a coordination of ~3 at 2.16 and 2.18 Å, respectively. Following the first two shells repeating V-Fe and V-S backscatters were fit corresponding to the structure of mackinawite, similar to Ikogou et al. (2017).

3.5. Environmental Implications

Vanadate removal at circumneutral pH under anoxic conditions by Fe(II)-bearing minerals can involve sorption, reduction, and, in the case of mackinawite, structural incorporation. This work demonstrates the ability for Fe(II)-bearing phases to sorb and reduce V(V) to V(IV), effectively removing bioavailable V from solution through the formation of inner-sphere surface complexes or incorporation into mineral structures. While rates of removal and reduction differ between Fe(II) mineral phases, reduction of V(V) to V(IV) occurs during reaction with magnetite, siderite, and mackinawite phases. Increased removal rates and V sorption capacity onto mineral surfaces under anoxic conditions can be summarized as follows: mackinawite > ferrihydrite ≥ siderite > magnetite >> pyrite. Reaction with $Fe^{2+}_{(aq)}$ was slow compared to V(V) removal *via* magnetite, siderite, mackinawite, and ferrihydrite (Figure A.2). Aqueous Fe^{2+} may, however, enhance V(V) removal over longer times via surface complexation or co-precipitation with secondary Fe precipitates. Overall, V(V) forms bidentate edge- and corner-sharing complexation in the case of ferrihydrite, consistent with sorption of other oxyanions onto iron (oxyhydr)oxide surfaces (Manceau, 1995). Whereas V sorption onto magnetite showed edge- and corner-sharing surface complexes with partial reduction of $H_2V^VO_4^-$ to $V^{IV}O^{2+}$ at the magnetite surface. Similarly, V(V) removal by siderite produced a mixture of V(V) and V(IV) species, dominated by V(IV), which formed bidentate corner-sharing complexes, and, at early reaction times, monodentate mononuclear complexes. In the case of $Fe^{2+}_{(aq)}$, V uptake was limited after 8 h and approached 47% removal following 48 h. The incorporation of V into tetragonal mackinawite structure is enhanced by its low solubility (K_{sp} = -3.5) releasing H_2S^0, HS^-, S^{2-} enhancing the ability for aqueous V to complex and coprecipitate within FeS (Couture et al., 2013; Wolthers et al., 2005a). This structural incorporation of V(IV) and V(III) into mackinawite may provide a low-temperature mechanism for V sequestration by Fe(II)-sulfides in anoxic environments (Tribovillard et al., 2006; Wanty and Goldhaber, 1992). Inner sphere complexation and incorporation reactions with Fe(II) minerals forms strong complexes limiting bioavailability of V(V) and may effectively inhibit mobility over geologic-time scales. Results demonstrate that V redox cycling at oxic-anoxic interfaces, for example water-sediment interface in lakes or saturated-unsaturated interface in soils, may have important implications for V mobility and, potentially, toxicity in the environment (Nesbitt and Lindsay, 2017; Shaheen et al., 2019; Wright et al., 2014).

3.6. Acknowledgements

Funding was provided by the Natural Sciences and Engineering Council of Canada (NSERC) through the Discovery Grants program (Grant No. RGPIN-2014-06589). Additional support awarded to CJV through NSERC – Canada Graduate Scholarship – Masters (NSERC CGS-M) Program. A portion of the research described was performed at the Canadian Light Source, which is supported by the Canada Foundation for Innovation, NSERC, the University of Saskatchewan, the Government of Saskatchewan, Western Economic Diversification Canada, the National Research Council, and the Canadian Institutes of Health Research. Contributions to this manuscript consist of myself and Dr. Matthew Lindsay, where I conducted laboratory experiments and analytical work, and we both contributed to the experimental design, data analysis, and manuscript preparation. I thank Dr. R.-M. Couture for assistance with multi-reaction modeling setup and M. Cowell, N. Galuschik, D. Meili, and J. Schulte for assistance during experimental sampling.

CHAPTER 4: SORPTION OF (POLY)VANADATE ONTO FERRIHYDRITE AND HEMATITE: AN *IN-SITU* ATR-FTIR STUDY

4.1. Abstract

Vanadium (V) contamination is an emerging environmental concern due to increased use in industrial activities and growing anthropogenic release from fossil fuel emissions and mine wastes. Iron (oxyhydr)oxides are important sinks for contaminants including V, yet adsorption mechanisms of polymeric V species have yet to be described. Here I identify the ability for ferrihydrite and hematite to attenuate aqueous (poly)vanadate species *via* surface complexation between pH 3 and 6 using *in situ* attenuated total reflectance – Fourier transform infrared spectroscopy. At low surface loadings and mildly acidic pH (i.e., 5 and 6), $H_2VO_4^-$ adsorption onto ferrihydrite and hematite surfaces results from formation of inner-sphere complexes. At higher $[V]_T$ and mildly acidic pH, adsorbed polynuclear V species in this study include $H_2V_2O_7^{2-}$ and $V_4O_{12}^{4-}$. Whereas, $HV_{10}O_{28}^{6-}$, $H_3V_{10}O_{28}^{5-}$, and $NaHV_{10}O_{28}^{4-}$ are the predominant adsorbed species under acidic conditions (i.e., 3 and 4) and at elevated $[V]_T$. Surface polymers were identified on hematite at all experimental pH values, whereas polymeric adsorption onto ferrihydrite was limited to pH 3 and 4. Adsorption isotherms illustrate the low affinity of polyvanadate species for ferrihydrite surfaces at pH 5 and 6 compared to hematite. This result suggests that the higher crystallinity of hematite offers a more suitable substrate for polymer formation compared to ferrihydrite at circum-neutral pH. Here I analyze the capacity for polymeric V species to adsorb at Fe(III) (oxyhydr)oxide surfaces and to subsequently form surface polymers, which has implications for understanding V bioavailability, behaviour, and fate in the environment.

4.2. Introduction

The complex aqueous speciation of vanadium (V) makes V a unique trace metal for studying Earth's natural processes (Babechuk et al., 2019; Baes and Mesmer, 1976; Shaheen et al., 2019; Tribovillard et al., 2006). Elevated V concentrations (>10,000 mg kg^{-1}) are commonly associated with primary ore minerals and secondary phases in bauxite, phosphate, coal, black shales, and

crude oil deposits at elevated concentrations (Brinza et al., 2015; Kaur et al., 2009; Schwertmann and Pfab, 1994; Wanty and Goldhaber, 1992). Vanadium is known to be acutely toxic to organisms and has recently been listed as a contaminant of concern due to increased anthropogenic release from industrial (i.e., steel byproducts or catalytic chemistry) and mining activities (Aureliano et al., 2013; Aureliano and Crans, 2009; Larsson et al., 2013; Schlesinger et al., 2017; Watt et al., 2018). Vanadium is listed on the Contaminant Candidate List 4,(USEPA, 2016) yet few jurisdictions have established water quality guidelines (e.g., Canada and the Netherlands) (Environment and Climate Change Canada, 2016; RIVM Letter Report 601714021/2012; National Institute for Public Health and the Environment, 2012). Background aqueous V concentrations range from 0.0005 to 180 μg L^{-1} depending on the weathering rates and source material; however, concentrations exceeding 3 mg L^{-1} can occur in mining environments (Burke et al., 2012; Hudson-Edwards et al., 2019; Nesbitt and Lindsay, 2017).

Aqueous V speciation is highly dependant on redox conditions, pH, total vanadium concentration ($[V]_T$) and ionic strength (I), with a variety of monomeric and polymeric species possible under different conditions (Baes and Mesmer, 1976; Chen and Liu, 2017; Wanty and Goldhaber, 1992). Under oxic conditions, V(V) dominates and forms monomeric ($[H_xVO_4]^{(3-x)-}$) and polymeric (e.g., $[H_xV_{10}O_{28}]^{(6-x)-}$) aqueous species. With increasing $[V]_T$, oligomerization and condensation reactions transform monomeric vanadate into dimers ($[H_xV_2O_7]^{(4-x)-}$), trimers ($V_3O_{10}^{5-}$), tetramers ($V_4O_{12}^{4-}$), pentamers ($V_5O_{15}^{5-}$), hexamers ($V_6O_{18}^{6-}$), and decamers ($[H_xV_{10}O_{28}]^{(6-x)-}$) between pH 2 and 10. At low (< 3) and high (> 9) pH, polynuclear species decompose to form VO_2^+ and HVO_4^{2-}, respectively. Unlike molybdenum (Mo) and tungsten (W) polynuclear species, polyvanadate species maintain tetrahedral coordination, with the exception of octahedral decavanadate. Aqueous polyvanadate species maintain a corner-sharing VO_4 tetrahedra connected by bridging O atoms, and $V_4O_{12}^{4-}$, $V_5O_{15}^{5-}$, and $V_6O_{18}^{6-}$ form cyclical structures (Aureliano and Crans, 2009; Cruywagen, 1999). In comparison, the decavanadate structure includes three distinct octahedral sites (Aureliano and Crans, 2009; Baes and Mesmer, 1976; Cruywagen, 1999). Decavanadate includes six V atoms in the middle, two of which are in the center (site a) and differ from the other four surrounding V atoms (site b), these six atoms are then capped by two atoms at the top and bottom (site c).

Iron (Fe) (oxyhydr)oxides are a key control on element mobility and bioavailability in soils and sediments (Cornell and Schwertmann, 2003). These phases exhibit a high affinity for uptake

of oxyanion-forming elements, including V, by sorption or incorporation reactions (Brinza et al., 2019, 2015; Kaur et al., 2009; Larsson et al., 2017; Peacock and Sherman, 2004; Schwertmann and Pfab, 1994; White and Peterson, 1996). Sorption of mononuclear vanadate species onto Fe (oxyhydr)oxides results from formation of inner-sphere bidentate corner- and edge-sharing surface complexes (Brinza et al., 2019; Larsson et al., 2017; Peacock and Sherman, 2004). While aqueous vanadate sorption by Fe(III) (oxyhydr)oxides has been described previously in field and laboratory settings (Brinza et al., 2019, 2015, 2008; Hudson-Edwards et al., 2019; Larsson et al., 2017; Mayes et al., 2011; Peacock and Sherman, 2004; Wisawapipat and Kretzschmar, 2017), the interaction of polynuclear V species with these phases has not been examined. Nevertheless, these reactions likely impact V mobility in terrestrial waters characterized by elevated $[V]_T$. Previous experimental work on polynuclear Mo(VI), W(VI), and U(VI) uptake by Fe(III) (oxyhydr)oxides and layered double hydroxides has utilized *in situ* attenuated total reflectance-Fourier transform infrared (ATR-FTIR) spectroscopy to discriminate between the various aqueous and adsorbed polymeric species (Davantès et al., 2016, 2015; Davantès and Lefèvre, 2015, 2013; Lefèvre et al., 2006). For example, attenuation of mono and polynuclear Mo(VI) species by hematite occurred through monodentate, bidentate, and tridentate sorption complexes, and additionally formed surface polymers by epitaxial growth on crystalline (0001) hematite surfaces (Davantes et al., 2017). Formation of surface polymers at Fe(III) (oxyhydr)oxide surfaces can inhibit the adsorption of inorganic contaminants and, therefore, decrease the reactivity of natural iron phases (Christl et al., 2012; Hu et al., 2015; Sun and Bostick, 2015).

Several studies have considered vanadate ($H_2VO_4^{2-}$) adsorption and incorporation with 2-line ferrihydrite and hematite by EXAFS analysis (Brinza et al., 2015; Larsson et al., 2017), yet uptake of polyvanadate species has not previously been considered. Here I compare the uptake of aqueous (poly)vanadate species by 2-line ferrihydrite and hematite [α-Fe_2O_3] phases using *in situ* ATR-FTIR spectroscopy over a range of pH (i.e., 3 to 6) and $[V]_T$ (i.e., 50 to 5000 µM). Thermodynamic modelling was used to assess relative proportions of (poly)vanadate species and, therefore, to assist with interpretation of ATR-FTIR results. Analysis of molecular-level reactions between aqueous monomeric, oligomeric, and polymeric species and mineral surfaces by ATR-FTIR is a well-established technique (Davantès and Lefèvre, 2015; Hu et al., 2015; Mayordomo et al., 2018; Myneni et al., 1998; Peak et al., 2003; Wang et al., 2018). My results

contribute new information on aqueous (poly)vanadate attenuation by Fe(III) (oxyhydr)oxides and improve understanding of processes controlling environmental V mobility.

4.3. Materials and Methods

4.3.1. Materials and Synthesis

Solutions were prepared using ultra-pure water (18.2 MΩ cm^{-1} resistivity) that was boiled for 15 min, cooled, and purged with $N_{2(g)}$ for 24 h in an anoxic chamber (Coy Laboratories, 5% H_2 balanced with N_2) to limit dissolved CO_2 during ATR-FTIR experiments. A stock solution containing 5000 µM V was prepared by dissolving high purity (>99.0%) sodium orthovanadate (Na_3VO_4) in a 0.05 M NaCl background electrolyte. This stock solution was then diluted to produce a range of $[V]_T$: 50, 100, 250, 500, 750, 1000, 3000, and 5000 µM. The pH of these solutions were then adjusted with 0.1 and 1.0 M trace-metal grade HCl to pH (± 0.1) 3, 4, 5, or 6.

Ferrihydrite and hematite synthesis followed methods described by Cornell and Schwertmann (2003) and Al-Kady et al. (2011) with slight modifications. Briefly, ferrihydrite was synthesized by dissolving 40 g of $FeCl_3$ in 500 mL of deionized (DI) water and titrated with 1.0 M NaOH to pH 7.5 and stirred vigorously for 1 h. Hematite was prepared by dissolving $FeCl_3$ in boiling deionized water, which was allowed to react for 30 min, at which time concentrated NaOH was added until pH stabilized at pH 7 and allowed to cool at room temperature. The resulting ferrihydrite and hematite suspensions were centrifuged and rinsed at least 3 times with DI water to remove residual ions. The solids were then resuspended in 0.05 M NaCl electrolyte to achieve a 10 g L^{-1} mineral slurry. The mineralogy of synthesized phases was confirmed by powder X-ray diffraction.

4.3.2. In situ ATR-FTIR Isotherm Experiments

The ATR-FTIR spectra were collected on an Invenio-R FTIR spectrometer (Bruker Corp., USA) equipped with an N_2-cooled Mercury-Cadmium-Telluride (MCT) detector. Measurements were collected with a Bruker Platinum ATR with a single-bounce ZnSe/diamond internal reflective element (IRE) with a 45° incidence angle. The instrument and sample compartments were continuously purged with dry air. Spectra represent an average of 512 scans collected at 4 cm^{-1} resolution. Collected FTIR spectra were truncated between 620 to 1010 cm^{-1}, baseline corrected, and integrated using OPUS v.8.1 software. The truncation limits selected to minimize distortion from baseline correction and to avoid interference of unavoidable bands from H_2O and Fe

(oxyhydr)oxide present below ~600 cm^{-1}. At 667 cm^{-1} a small negative band for CO_2 is present, but overall does not affect the interpretation or deconvolution fits for adsorbed spectra.

Initial spectra were collected for aqueous V samples at 5000 µM for pH 1, 4, 7, and 11. The selected pH values were selected to observe aqueous VO_2^+, $H_xV^VO_4^{(3-x)-}$, and polynuclear species, which correspond to distinct IR bands. A background scan was obtained for the 0.05 M NaCl background electrolyte and sample spectra were then collected by dropping aqueous V samples onto the IRE. Adsorption isotherm experiments were performed by equilibrating V(V) solutions (50 to 5000 µM) with ferrihydrite and hematite films under constant flow. Films deposited on the ATR crystal were done by drop casting 10 µL of prepared mineral suspensions (10 g L^{-1}) and dried under continuous flow of $N_{2(g)}$ until no residual water was apparent. The drop casting procedure was repeated until complete coverage of the IRE was achieved. Following deposition of ferrihydrite or hematite, the 0.05 M NaCl background solution was passed over the film at a constant rate of 1.3 mL min^{-1} using a peristaltic pump, this process was repeated for each pH. An initial background spectrum was collected, and spectra were then recorded every 2 min until the film reached equilibration with the electrolyte, noticed by lack of changes in the spectra. Following equilibration, a final background spectrum was collected and vanadate solutions were continuously passed over the film at the appropriate concentration, from low (50 µM) to high (5000 µM) $[V]_T$. Sorption onto ferrihydrite and hematite at each concentration was monitored by collecting spectra every 60 s until no change in spectra was noted (20 to 30 min. At this time the next highest V solution was passed through the setup. Band positions were chosen by 2nd derivative analysis of each spectra at the given pH conditions. Vanadium sorption isotherms were produced by integrating processed spectra for each given pH condition following reaction with ferrihydrite and hematite films. Integrated isotherm areas for each system were fit using the Langmuir isotherm equation by inverse modeling to minimize the root-mean-square error (RMSE). Deconvolution of spectra was achieved by fitting the minimum number of Gaussian peaks using the Origin software package (Origin V.2016).

4.3.3. Aqueous Speciation Modeling

Thermodynamic equilibrium modeling of aqueous V species was performed using the PHREEQCi (Version 3.1.5) code (Parkhurst and Appelo, 2013) with a modified Minteq version 3.1 database (Gustafsson, 2018). Mononuclear and polynuclear V protonation reactions and constants were also considered from Baes and Mesmer (1976), Chen and Liu (2017), Cruywagen

et al. (1996), Cruywagen (1999), Elvingson et al. (1996), Larson (1995), and Wanty and Goldhaber (1992). Aqueous Na-decavanadate ($NaH_xV_{10}O_{28}^{(5-x)-}$) complexes can represent up to ~40 % of the total V species at 5000 µM and low ionic strength (I = 0.05 M), and were therefore considered in thermodynamic modeling (Chen and Liu, 2017).

4.4. Results

4.4.1. ATR-FTIR Spectra

Initial aqueous V spectra collected at pH 1, 4, 7, and 11 displayed distinct features associated with the VO_2^+, $H_xV^VO_4^{(3-x)-}$, and polynuclear species (Figure 4.1 and B.2) and were consistent with literature values summarized in Table 4.1. A broad band at 1187 cm^{-1} with weak shoulders at 938 and 1015 cm^{-1} is apparent in spectra for the pH 1 solution. Spectra collected for the pH 4 solution exhibit weak bands at 842, 965, and 1016 cm^{-1}, whereas at pH 7 bands were present at 834, 952, and 1066 cm^{-1}. A single band is present at 861 cm^{-1} in spectra obtained for the pH 11 solution.

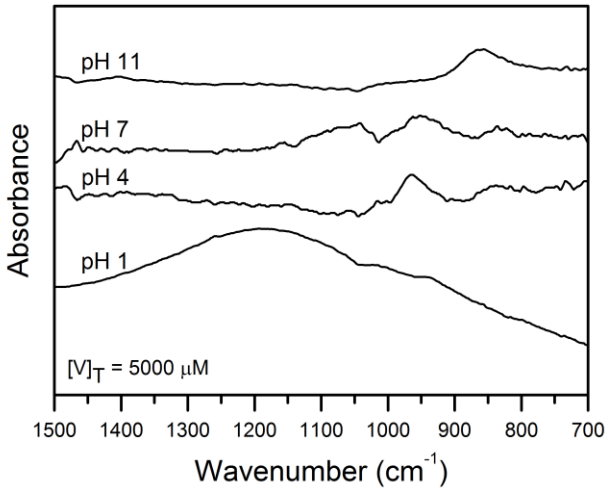

Figure 4.1. ATR-FTIR spectra for aqueous V solutions (5000 µM) at pH 11, 7, 4, and 1.Spectra at pH 4 and 7 were enhanced by 3x.

Multiple bands appeared in the spectra obtained during vanadate sorption onto ferrihydrite and hematite from pH 3 to 6 (Figure 4.2). Band positions were determined from minimums in the 2nd derivative of adsorbed spectra and optimized by deconvolution fits (Figure 4.3 and B.2; Table B.1). Vanadium adsorption onto ferrihydrite produced broader spectral features and fewer bands regardless of concentration (Figure 4.2). Multiple bands are apparent at 660, 711, 764, 815, 885, and 935 cm^{-1} at pH 6 following reaction with ferrihydrite. The bands at 660, 711, and 764 cm^{-1}

exhibit relatively consistent position and intensity across all pH values, whereas bands positioned between 800 and 1000 cm^{-1} shift to higher frequencies with decreasing pH. This trend also corresponds to new bands at 977 cm^{-1} (pH 3) and 970 cm^{-1} (pH 4) that increase in intensity compared to bands at lower frequencies as pH decreases and at elevated $[V]_T$ (Figure B.1).

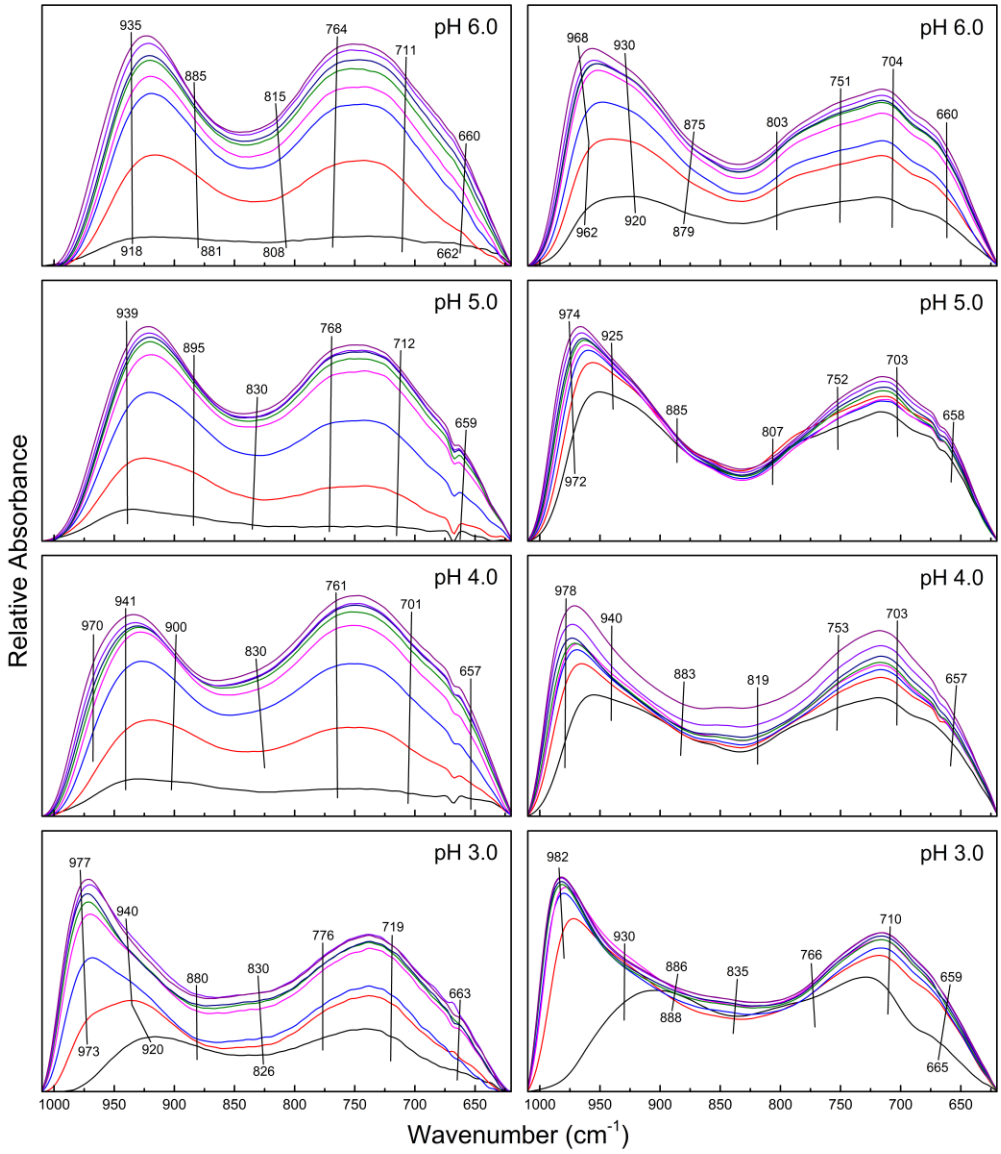

Figure 4.2. ATR-FTIR spectra of sorbed V(V) onto ferrihydrite (left column) and hematite (right column) from 50 (bottom) to 5000 (top) µM. Black lines represent selected peak positions based on qualitative analysis using the 2nd derivative and deconvolution peak fitting for spectra collected at 5000 µM.

In contrast to ferrihydrite, adsorption onto hematite surfaces displays similar bands independent of pH and surface loadings. Spectra obtained at pH 6 exhibit bands at approximately

660, 704, 751, 803, 875, 930, and 968 cm^{-1} (Figure 4.2). These seven bands are present from pH 3 to 6), and from low (50 µM) to high (5000 µM) $[V]_T$. With increased surface loading and decreasing pH, peaks at 930 and 968 cm^{-1} grow systematically in intensity while bands between 620 to 800 cm^{-1} remain relatively constant until pH 3. At which point bands at positions 660, 710, and 766 cm^{-1} are present, compared to the numerous bands between pH 4 and 6.

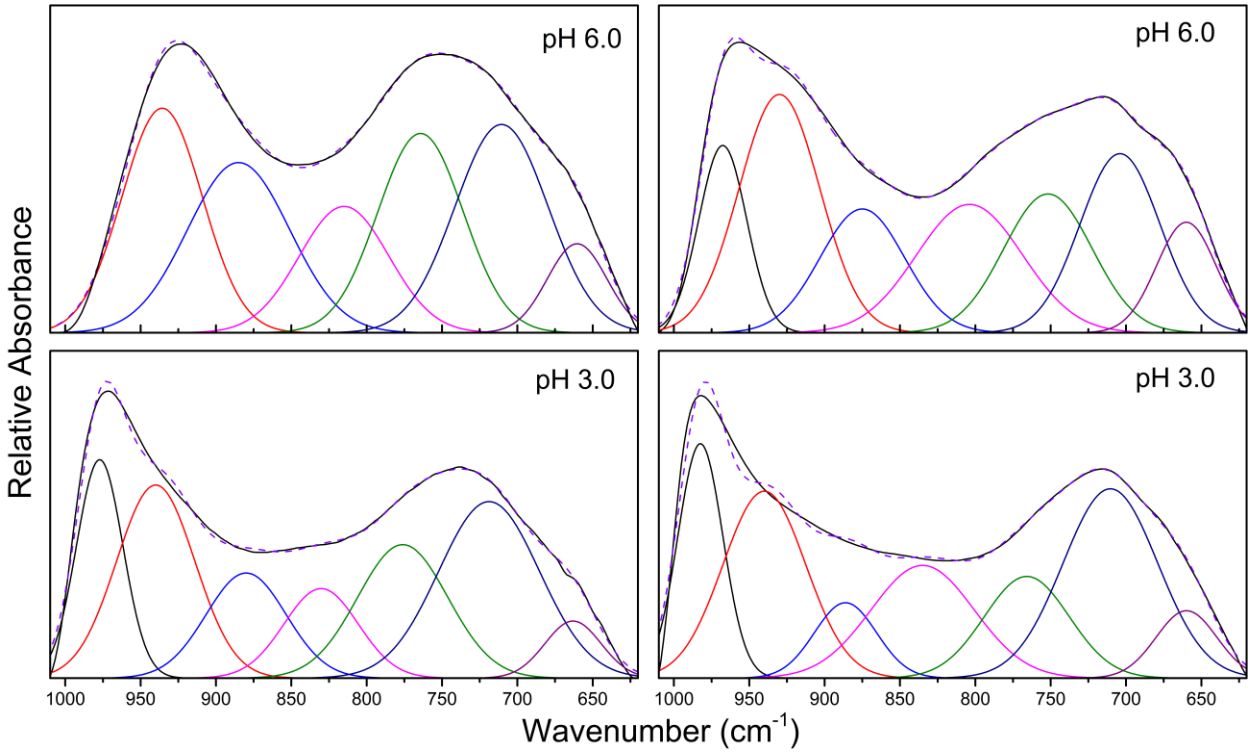

Figure 4.3. Decomposition of ATR-FIR spectra for adsorbed V(V) onto hematite (left column) and ferrihydrite (right column) at 5000 µM.

4.4.2. Adsorption Isotherms

Langmuir isotherm fits consistently show larger partitioning coefficients (K) for hematite than that for ferrihydrite (Table B.2). Optimal isotherm fits for hematite produced fit constants ranging from 0.012 to 0.100, whereas K values for ferrihydrite isotherms were significantly smaller, 0.005 to 0.007 (Table B.2). These K values suggest that (poly)vanadates have a higher affinity for hematite surfaces compared to ferrihydrite. Isotherms for ferrihydrite experiments showed no apparent pH-dependent trends and produced coefficients consistent among all experiments (Figure 4.4a). Although K values varied among experiments for hematite, a decrease in K values from 0.100 to 0.023 corresponded to a pH decrease from 5 to 3. The pH 6 experiment for hematite does not follow this trend, yet the K value is similar to (poly)vanadate partitioning

coefficients onto ferrihydrite at all experimental pH values. This result indicates that at pH 6, (poly)vanadate ions exhibit similar affinity for sorption onto hematite and ferrihydrite. At high V concentrations (> 1000 µM) there is greater variability in the normalized absorbance and isotherms are poorly described by the Langmuir model for pH 4 and 5 isotherms following reaction with the hematite films (Figure 4.4b). This deviation from the fit at pH 4 and 5 may result from adsorption of multiple energetically heterogeneous species, which the Langmuir model cannot effectively describe.

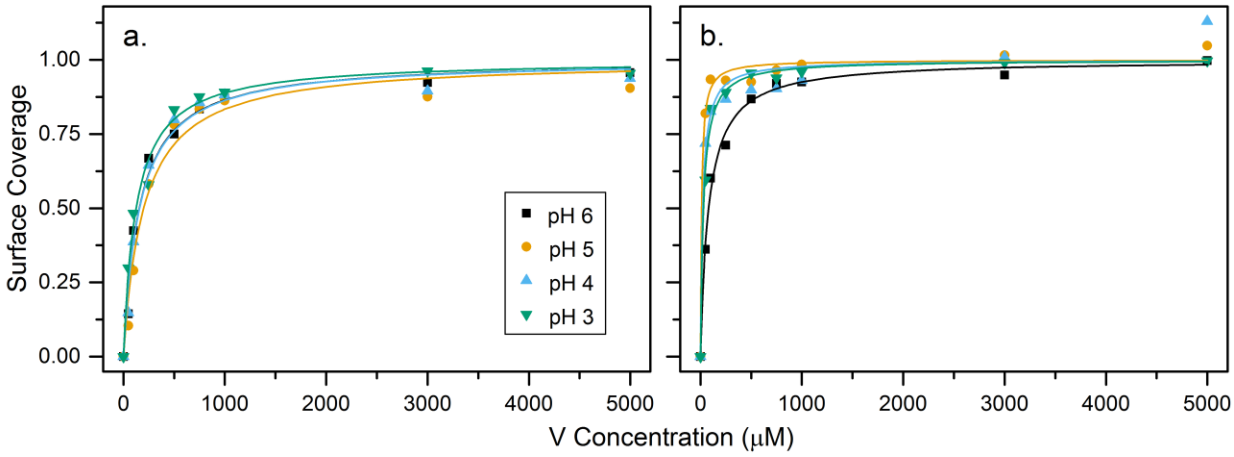

Figure 4.4. Integrated absorbance isotherms for ferrihydrite (a) and hematite (b) with modeled Langmuir isotherm fits (solid lines).

4.5. Discussion

4.5.1. Aqueous (Poly)Vanadate Speciation

Previous studies have observed several active Raman and IR bands for aqueous (poly)vanadate species and adsorbed species onto layered double hydroxide phases (Table 4.1). Features observed in ATR-FTIR spectra from this study (Figure 4.1) can be interpreted by comparing relative proportions of each V(V) species with these published values (Figure 4.1). This comparison indicates that VO_2^+, $[H_xV_{10}O_{28}]^{(6-x)-}$, chain-like forming species (i.e., $[H_xV_2O_7]^{(4-x)-}$ and $V_4O_{12}^{4-}$), and HVO_4^- dominate at pH 1, 4, 7, and 11, respectively. Under highly acidic conditions (i.e., pH < 2), VO_2^+ dominates and is identified by bands at 938, 1015, and 1187 cm^{-1} (Figure 4.1). Griffith and Lesniak (1969) ascribed bands at 920, and 940 cm^{-1} to VO_2^+ at pH 0.9, which is generally consistent with the weak band measured at 938 cm^{-1} here. With a similar linear structure to the uranyl cation ($O=U=O^{2+}$), aqueous VO_2^+ spectra can be described by asymmetric stretching of V=O bonds (Gückel et al., 2013; Lefèvre et al., 2006).

Table 4.1. Summary of dissolved V species band positions measured by Raman (*) and IR (†) spectroscopy. Peak positions for $H_2V_2O_7^{2-}$ and $V_4O_{12}^{4-}$ are reported with identical values as these species occur simultaneously in solution and cannot be determined separately. Metavanadate species included are $V_3O_{10}^{5-}$, $V_4O_{12}^{4-}$, $V_5O_{15}^{5-}$, and $V_6O_{18}^{6-}$.

References	VO_2^+	VO_4^{3-}	HVO_4^{2-}	$H_2VO_4^{2-}$	$[H_xV_2O_7]^{(4-x)-}$	Metavanadate	$H_xV_{10}O_{28}^{(6-x)-}$
1†	938, 1015, 1187		861	952	834, 952	834, 952, 1066	842, 965, 1016
2*		820	875		875	947	593, 967, 995
3†		336, 804, 826			360-464, 560, 760-790, 830-895, 915-950	646, 940	
4, 5*		827	351, 545, 877	945	351, 503, 810, 850, 877	360, 884, 945	320, 454, 534, 595, 800, 834, 870, 960-998
6, 7, 8*†	920, 940	340, 780, 827	351, 545, 800, 877		210, 351, 503, 810, 850, 877, 915	330, 360, 490, 630, 905, 945	910, 955, 960, 990

1 This study
2 Aureliano et al. (2016)
3 Salak et al. (2012)
4 Twu and Dutta (1990)
5 Twu and Dutta (1989)
6 Griffith and Lesniak (1969)
7 Griffith (1967)
8 Griffith and Wickins (1966)

Thermodynamic modeling predicts that $H_2VO_4^{2-}$ dominates between pH 5 and 9 when $[V]_T$ is below 1000 µM. However, at pH 6 the linear molecule $H_2V_2O_7^{2-}$ and cyclical $V_4O_{12}^{4-}$ polyvanadate species may constitute ~30 % of $[V]_T$ (Figure 4.5). This modeling also predicts that when $[V]_T$ is 5000 µM, $H_2VO_4^-$, $H_2V_2O_7^{2-}$ and $V_4O_{12}^{4-}$ account for approximately 20, 15 and 60 % of the total, respectively. Measured spectra (Figure 4.1) show similar features to previously published IR spectra for both aqueous and complexed species within layered double hydroxide interlayers (Table 4.1). Bands at 834, 952, and 1066 cm^{-1} correspond to $H_2VO_4^-$, $H_2V_2O_7^{2-}$, and $V_4O_{12}^{4-}$ since they have a similar C_{2v} symmetry and V-O-V or V-O stretching modes (Griffith and Lesniak, 1969; Griffith and Wickins, 1966; Salak et al., 2012; Twu and Dutta, 1990, 1989). With decreasing pH, the major species become $HV_{10}O_{28}^{6-}$, $H_3V_{10}O_{28}^{5-}$ and $NaHV_{10}O_{28}^{4-}$ polymers

(Figure 4.5), which produce bands at 842, 965 and 1016 cm^{-1}, respectively. Decavanadate has a similar structure to the $Mo_7O_{24}^{6-}$ polyoxyanion with both species shown to have C_{2v} symmetry in a distorted octahedral geometry and bands occurring between 800 and 1000 cm^{-1} (Cruywagen, 1999; Davantes et al., 2017; Davantès and Lefèvre, 2013; Griffith and Lesniak, 1969). Vanadate polymers decompose at pH above 10 to form the HVO_4^- oxyanion, which exhibits C_{3v} symmetry. The measured value of 861 cm^{-1} at pH 11 is consistent with HVO_4^- Raman and IR values at 877 cm^{-1} (Aureliano et al., 2016; Griffith and Wickins, 1966; Twu and Dutta, 1990, 1989). The free T_d VO_4^{3-} is only present at pH above 12, but similar to other aqueous oxyanion forming metals (e.g., Mo and W) exhibits only a single band at ~830 cm^{-1} (Table 4.1) (Davantès and Lefèvre, 2015).

4.5.2. Attenuation of (Poly)Vanadate Species

Surface adsorption of aqueous oxyanions alters the symmetry of the free species resulting in a lower symmetry indicative of surface complexation (Davantès and Lefèvre, 2015; Hug, 1997; Myneni et al., 1998; Nakamoto, 1997; Peak et al., 2003, 1999). Sorption of V onto ferrihydrite surfaces produced four strong bands between 650 and 850 cm^{-1} that are pH-independent, and three distinct bands between 850 and 980 cm^{-1} that exhibit increasing intensity with decreasing pH (Figures 4.3, 4.4). Deconvolution and 2nd derivative analysis of ferrihydrite spectra reveal limited differences for pH 4 and 6, whereas spectra collected at pH 3 exhibit a sharp increase in intensity at 970 cm^{-1} (Figure B.2). At low $[V]_T$ (< 500 µM), peaks are distinguishable at approximately 880 and 940 cm^{-1} suggesting the presence of minor amounts (~10 to 15%) of polynuclear V(V) species (Figure 4.2). Bands reflecting adsorption of polynuclear V species (i.e., 900, 940, and 970 cm^{-1}) increase in intensity at elevated $[V]_T$ and decreasing pH (Figure 4.3; Figure B.2) (Griffith and Lesniak, 1969; Griffith and Wickins, 1966; Salak et al., 2012). A concomitant decrease in band intensity associated with tetrahedrally coordinated (poly)vanadate sorption (650 and 850 cm^{-1}) is also apparent.

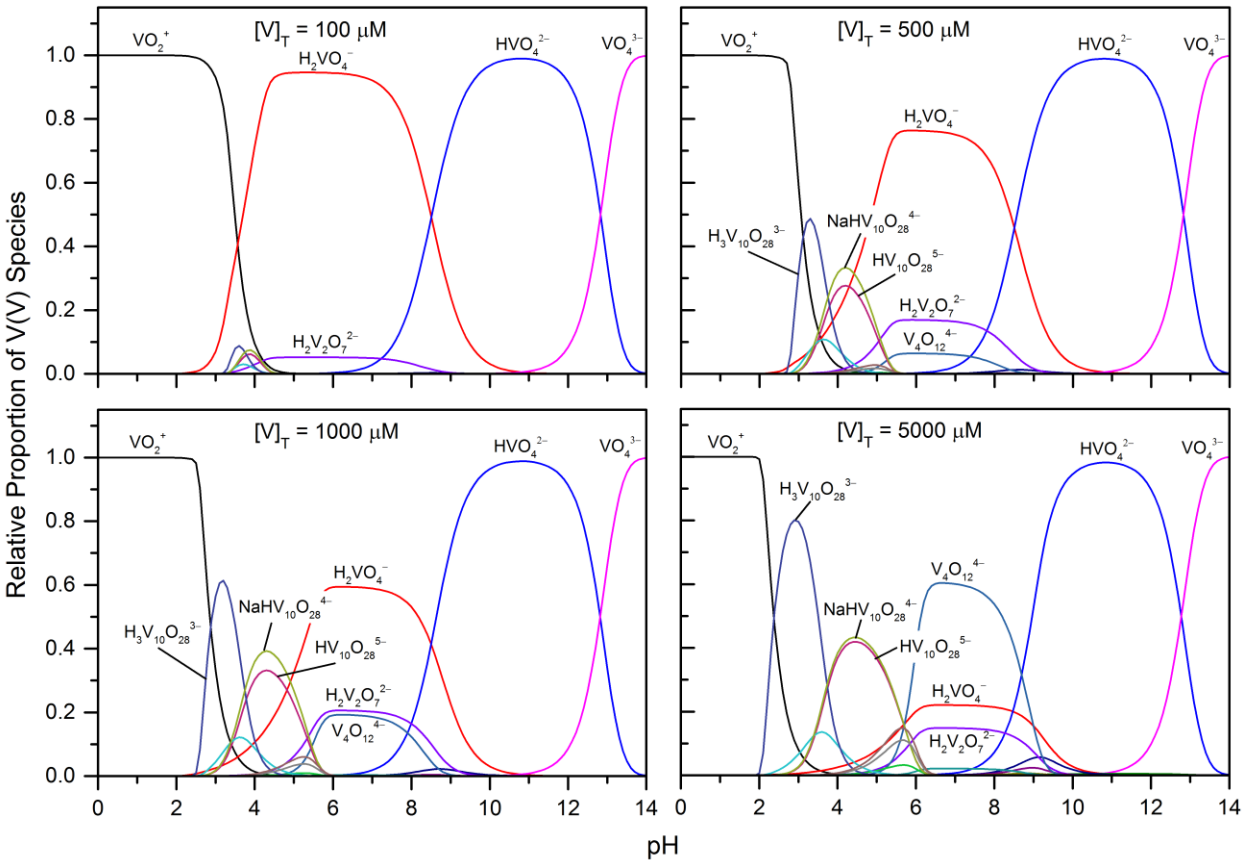

Figure 4.5. Aqueous V speciation diagrams at 100 (top left), 500 (top right), 1000 (bottom left), and 5000 (bottom right) µM based on compiled thermodynamic data.

Comparatively, surface adsorption of V at hematite surfaces produces sharper features with five main bands between 650 and 860 cm^{-1} and three bands between 850 and 950 cm^{-1} (Figure 4.2 and 4.3). Similar to adsorbed V spectra on ferrihydrite, bands at lower wavenumbers (650 to 860 cm^{-1}) result from surface complexation of tetrahedrally coordinated (poly)vanadate species. These features are generally sharper at pH 5 and 6 but weaken or disappear as pH decreases below 4 (Figure 4.2). The two dominant bands at approximately 930 and 970 cm^{-1} systematically increase in intensity with higher surface loadings. However, as pH decreases from 6 to 3 the peak at ~930 cm^{-1} is gradually dampened by the intense peak at 970 cm^{-1}.

When considering V sorption onto ferrihydrite and hematite surfaces, the appearance and dampening of bands directly relates to aqueous (poly)vanadate speciation and surface complexation. At $[V]_T$ less than 1000 µM and pH 5 and 6, the doubly protonated $H_2VO_4^-$ is the predominant specie. Assigning bands associated to V-O-Fe adsorption complexes on ferrihydrite and hematite surfaces at low $[V]_T$ is difficult due to several adsorption complexes, mixtures of

adsorbed species, and the C_{2v} symmetry of $H_2VO_4^-$ (Nakamoto, 1997). Adsorption of $H_2VO_4^-$ onto Fe(III) and Al(III) (oxyhydr)oxides results from formation of inner-sphere bidentate binuclear and mononuclear complexes (Brinza et al., 2019, 2015; Larsson et al., 2017; Peacock and Sherman, 2004; Wehrli and Stumm, 1989). Therefore, peaks produced during $H_2VO_4^-$ adsorption at pH 5 and 6 likely produce band splitting similar to bidentate surface complexation of arsenate ($H_2AsO_4^{2-}$) on (oxyhydr)oxides (Hu et al., 2015; Myneni et al., 1998; Roddick-Lanzilotta et al., 2002). However, at increased concentrations, $H_2V_2O_7^{2-}$ and $V_4O_{12}^{4-}$ polymers dominate aqueous speciation (Figure 4.5). Adsorption of these polyvanadate species at hematite surfaces produce bands at 930 and 968 cm^{-1} with that increase with $[V]_T$ (Figure 4.2 and B.2). The indiscernible bands at 970 cm^{-1} at pH 5 and 6 suggests that ferrihydrite may have a limited ability for surface polymer formation, due to its more amorphous characteristics. The high affinity of tetrahedrally coordinated V(V) species for Fe(III) (oxyhydr)oxide surfaces at circumneutral pH suggests that hematite is a suitable substrate for $H_2V_2O_7^{2-}$ and $V_4O_{12}^{4-}$ adsorption (Brinza et al., 2019, 2015; Larsson et al., 2017). Adsorbed dimer and tetramer polymers likely result from multiple monodentate bonds, since bidentate complexation would be sterically hindered.

Under slightly acidic conditions (i.e., pH 3 to 5) and $[V]_T$ above 250 µM, thermodynamically predicts $HV_{10}O_{28}^{6-}$, $NaHV_{10}O_{28}^{5-}$ and $H_3V_{10}O_{28}^{5-}$ polynuclear species to be the dominant aqueous V(V) species (Figure 4.5). Increasing abundance of these species correspond to increasing IR band intensities between 970 and 980 cm^{-1}. However, ferrihydrite may be less thermodynamically favourable for surface polymerization compared to the hematite (0001) crystal face due to the rigid and large decavanadate atomic structure. This hypothesis is supported by a higher number of bands attributed to polymeric species on hematite (Figure 4.3) and to higher affinity of (poly)vanadates for hematite based on Langmuir isotherms (Figure 4.4; Table B.2). Preferential polymer formation at the hexagonal (0001) hematite crystal face compared to less crystalline Fe(III) (oxyhydr)oxides has previously been demonstrated for Mo and W sorption (Davantes et al., 2017; Davantès et al., 2016; Davantès and Lefèvre, 2016). Unlike polymolybdate, epitaxial growth of decavanadate on hematite is likely inhibited by its large structure (Davantes et al., 2017). However, previous studies have observed substitution of metavanadate and decavanadate species into layered-double hydroxides (Salak et al., 2012; Twu and Dutta, 1990, 1989). At concentrations below 250 µM, the oxycation VO_2^+ represents over 60% of $[V]_T$ at pH 3 (Figure 4.5). Uptake of VO_2^+ is likely limited due to the experimental pH being below the point of zero charge for Fe (oxyhydr)oxide surfaces,

resulting in a net positive surface charge (Cornell and Schwertmann, 2003). Adsorption of VO_2^+ at ferrihydrite and hematite surfaces likely includes outer-sphere interactions and potentially weak inner-sphere monodentate sorption. This observation is consistent with previous adsorption data for VO_2^+ onto goethite and δ-Al_2O_3 through ligand exchange of surficial hydroxyl groups (Peacock and Sherman, 2004; Wehrli and Stumm, 1989).

4.6. CONCLUSIONS

While previous studies have described vanadate adsorption onto ferrihydrite and goethite, uptake of polyvanadate species by Fe (oxyhydr)oxides have not yet been considered (Brinza et al., 2019; Larsson et al., 2017; Peacock and Sherman, 2004). Investigation of (poly)vanadate interaction with ferrihydrite and hematite by ATR-FTIR allowed for the identification of multiple bonding environments and inferred uptake mechanisms. Measured spectra coupled with thermodynamic modelling highlights the complex geochemical behaviour of aqueous V(V). In mildly acidic waters (i.e., pH 5 to 6) and low concentrations (i.e., $[V]_T$ < 500 µm), $H_2VO_4^-$ adsorption produces multiple bands between 650 and 850 cm^{-1} indicating the formation of monodentate and bidentate surface complexes at both ferrihydrite and hematite surfaces. Bands at 930 and 970 cm^{-1} persist at elevated concentrations where tetrahedral coordinated $H_2V_2O_7^{2-}$ and $V_4O_{12}^{4-}$ form surface polymers at hematite. The lack of bands at 970 cm^{-1} in ferrihydrite spectra suggest surface polymer formation is limited. At pH 3 to 4, a strong band at ~980 cm^{-1} indicates the presence of adsorbed decavanadate on ferrihydrite and hematite. Similar to Mo and W polynuclear species, octahedrally coordinated decavanadate adsorption is likely constrained to monodentate surface complexation owing to its large and rigid structure. Adsorption of VO_2^+ at low pH and low $[V]_T$ is limited to outer sphere and inner sphere monodentate adsorption (Peacock and Sherman, 2004; Wehrli and Stumm, 1989). Similar to adsorption of Mo and W polymers, results suggest attenuation of polynuclear V(V) species are inhibited onto less crystalline Fe (oxyhydr)oxide surfaces (e.g., ferrihydrite, lepidocrocite, and goethite) at moderate pH conditions (Davantes et al., 2017; Davantès et al., 2016; Davantès and Lefèvre, 2016). The observed stability of aqueous V polynuclear species over a wide pH range (3 to 8) may have implications for V mobility within mining environments and long-term waste storage facilities. Overall, these results demonstrate the ability of (poly)vanadate species to adsorb and form surface polymers at ferrihydrite and hematite surfaces Adsorption of V polymers at Fe(III) (oxyhydr)oxides have the

potential to passivate reactive $Fe(O,OH)_6$ octahedra and further inhibiting uptake of nutrients or metals (Christl et al., 2012; Davantes et al., 2017; Hu et al., 2015; Swedlund et al., 2010). Therefore, these reaction have implications for V mobility in terrestrial waters (Aureliano and Crans, 2009) and use as a paleoredox indicator (Tribovillard et al., 2006).

4.7. Acknowledgements

Funding was provided by the Natural Sciences and Engineering Council of Canada (NSERC) through the Discovery Grants program (Grant No. RGPIN-2014-06589). Additional support awarded to CJV through NSERC – Canada Graduate Scholarship – Masters (NSERC CGS-M) Program. This manuscript consists of five contributing authors including myself, Mojtaba Abdolahnezhad, Dr. Michael Schmidt, Dr. Matthew Lindsay, and Dr. Derek Peak. Data collection was performed by myself, Mojtaba Abdolahnezhad compiled and condensed thermodynamic data used in this study, and all authors contributed to experimental design, data analysis, and manuscript preparation.

CHAPTER 5: CONCLUSIONS AND RECOMMENDATIONS

Few studies have described molecular mechanisms influencing aqueous V interactions at mineral surfaces. Nevertheless, metal-mineral interactions at Fe mineral surfaces exert a strong control on the mobility, distribution and bioavailability of oxyanion-forming metal(loid)s in terrestrial waters. Many paleo-environments and modern systems contain prevailing anoxic conditions that influence mineral precipitation-dissolution and recrystallization reactions and, therefore, trace metal mobility within these environments. Results from Chapter 3 demonstrate the capacity for Fe(II)-bearing phases to adsorb and reduce bioavailable vanadate to less mobile V(IV) and V(III) species in anoxic settings. Likewise, Chapter 4 highlights adsorption mechanisms of polynuclear V(V) species at Fe(III) (oxyhydr)oxide surfaces under oxic conditions, and the subsequent affects on Fe(III) (oxyhydr)oxide surface characteristics. Both studies within this thesis contribute to the current understanding of V mobility in oxic and anoxic conditions and, more generally, fundamental geochemical reactions relevant to Earth processes.

My overall research goal was to elucidate fundamental controls that influence V mobility during reaction with Fe(II) and Fe(III)-bearing phases relevant to near surface environments. The outcomes of each objective composing this thesis (defined in Chapter 1.3) are addressed in this section.

5.1. Objective 1

In Chapter 3, I describe adsorption and reduction mechanisms for V, as $H_2V^VO_4^-$, during reaction with magnetite, siderite, pyrite, and mackinawite phases. Parallel experiments with ferrihydrite and $Fe^{2+}_{(aq)}$ (200 μM) were also characterized for comparison. Kinetic adsorption of $H_2V^VO_4^-$ onto Fe-phases was rapid, where rate of uptake followed the order of: mackinawite > ferrihydrite ≥ siderite > magnetite >> pyrite. Secondary precipitates were apparent in the siderite and $Fe^{2+}_{(aq)}$ reactions, XRD and TEM-EDX analysis suggests the presence of mixed Fe^{2+}/Fe^{3+} green rust and Fe(III) (oxyhydr)oxides. Siderite and mackinawite were found to remove ≥ 90 % $H_2V^VO_4^-$ after 3 h, whereas attenuation by magnetite was short-lived and removed ~50% of aqueous vanadate after 48 h. Vanadate was found to adsorb at ferrihydrite and magnetite surfaces

through edge- and corner-sharing bidentate complexes. Subsequently, reduction of adsorbed $H_2V^VO_4^-$ by surface-mediated electron transfer generated ~30 % adsorbed $V^{IV}O^{2+}$ after 48 h. In contrast, $H_2V^VO_4^-$ uptake by siderite and $Fe^{2+}_{(aq)}$ reaction products yielded bidentate corner-sharing complexes only, but resulted in nearly complete reduction of V(V) to V(IV). Mackinawite experiment resulted in complete reduction of V(V) to V(IV) and minor amounts of V(III), which were then incorporated into the FeS tetragonal structure. These results demonstrate the mineralogical controls Fe(II)-phases exert on aqueous V removal within anoxic conditions.

5.2. Objective 2:

Attenuation of monomeric and polymeric V(V) species by ferrihydrite and hematite were characterized in Chapter 4. In this study I utilized ATR-FTIR spectroscopy to produce adsorption isotherms were collected at pH values from 3 to 6 and a range of $[V]_T$ between 50 and 5000 µM. Spectra were compared to relative proportions of V species at a given pH, and Raman and IR data from literature to differentiate (poly)vanadate species adsorption. At pH 6, adsorbed species included $H_2VO_4^-$ at low concentrations (<500 µM), and $H_2V_2O_7^{2-}$ and $V_4O_{12}^{4-}$ at elevated $[V]_T$ (>500 µM). Formation of $H_2V_2O_7^{2-}$ and $V_4O_{12}^{4-}$ surface polymers on hematite is supported by growth in band intensity at 930 and 968 cm^{-1}, which likely adsorb through multiple monodentate bonds. However, the absence of a band at ~970 cm^{-1} during V adsorption onto ferrihydrite at pH 5 and 6 suggest surface polymer formation are inhibited. Between pH 3 and 5 at $[V]_T$ > 250 µM, adsorption of $HV_{10}O_{28}^{6-}$, $NaHV_{10}O_{28}^{5-}$, and $H_3V_{10}O_{28}^{5-}$ is apparent by increased peak intensity at 980 cm^{-1} for both ferrihydrite and hematite. Overall, adsorption of surface polymers at pH 5 and 6 is limited at ferrihydrite surface but increases with decreasing pH. Similar to other polynuclear forming metals, hematite is capable of adsorbing and forming surface polymers with (poly)vanadate species compared to ferrihydrite. This study shows the importance in considering polyvanadate adsorption onto Fe(III) (oxyhydr)oxides at circum-neutral and acidic pH conditions.

5.3. Recommendations for Future Work

The complexity of V biogeochemistry offers many opportunities into understanding metal-mineral interactions within natural and contaminated systems There remain many knowledge gaps regarding V mobility and its long-term fate within soils and sediments. Several recent review papers have identified knowledge gaps in V geochemistry that require advancement

(Gustafsson, 2019; Huang et al., 2015; Shaheen et al., 2019; Watt et al., 2018). Here, I expand on these ideas based on the studies presented in this thesis. The following areas of study are recommended for future work:

- Few studies have observed the coprecipitation of V(V), V(IV), and V(III) species with mineral phases (Brinza et al., 2015; Kaur et al., 2009; Schwertmann and Pfab, 1994). In Chapter 3, secondary precipitates were described as a result of coupled oxidation of Fe(II)-bearing phases or aqueous Fe^{+2} with V(V) reduction. Reactive secondary phases (e.g., layered double hydroxides or Fe(III) (oxy)hydroxides) likely have the capability to incorporate V(IV) and V(III) into structural sites; however, the stability of V incorporated into secondary phases have not been characterized.
- The mobility of V in sulfidic conditions is poorly understood and should be investigated (Crans et al., 2010; Wanty and Goldhaber, 1992). Thiometallate species (e.g., As, Mo and W) are known to be highly reactive with the potential to incorporate into sulfide mineral structures. In Chapter 3, incorporation of V(IV) and V(III) into the tetragonal mackinawite structure was observed. The incorporation of V into mackinawite may affect its transformation to stable phases (i.e., greigite or pyrite), as well as the fate of V over geologic time. Vanadium mobility in sulfidic conditions remains largely unknown and thiovanadate species have yet to be characterized.
- Prior to this study mineralogical controls on polyvanadate species have not been investigated. Polymeric species are known to adsorb to mineral surfaces and, therefore, can passivate reactive surfaces. Further studies are required to elucidate uptake mechanisms of polynuclear V species at mineral surfaces and their ability to compete with concurrent nutrients or contaminants.
- Dynamic redox studies should be conducted to analyze mineralogical and environmental controls on (poly)vanadate mobility. These experiments could examine the influence of changing environmental conditions (i.e., redox, temperature, saturation) to better constrain V reactivity and mobility. New methods to determinate aqueous V species could also be utilized (Li and Le, 2007; Wen et al., 2019).

REFERENCES

Al-Kady, A.S., Gaber, M., Hussein, M.M., Ebeid, E.Z.M., 2011. Structural and fluorescence quenching characterization of hematite nanoparticles. Spectrochim. Acta - Part A Mol. Biomol. Spectrosc. 83, 398–405. https://doi.org/10.1016/j.saa.2011.08.052

Aureliano, M., Crans, D.C., 2009. Decavanadate ($V_{10}O_{28}^{6-}$) and oxovanadates: Oxometalates with many biological activities. J. Inorg. Biochem. 103, 536–546. https://doi.org/10.1016/j.jinorgbio.2008.11.010

Aureliano, M., Fraqueza, G., Ohlin, C.A., 2013. Ion pumps as biological targets for decavanadate. Dalt. Trans. 42, 11770–11777. https://doi.org/10.1039/c3dt50462j

Aureliano, M., Ohlin, C.A., Vieira, M.O., Marques, M.P.M., Casey, W.H., Batista De Carvalho, L.A.E., 2016. Characterization of decavanadate and decaniobate solutions by Raman spectroscopy. Dalt. Trans. 45, 7391–7399. https://doi.org/10.1039/c5dt04176g

Babechuk, M.G., Weimar, N.E., Kleinhanns, I.C., Eroglu, S., Swanner, E.D., Kenny, G.G., Kamber, B.S., Schoenberg, R., 2019. Pervasively anoxic surface conditions at the onset of the Great Oxidation Event: New multi-proxy constraints from the Cooper Lake paleosol. Precambrian Res. 323, 126–163. https://doi.org/10.1016/j.precamres.2018.12.029

Baes, C.F., Mesmer, R.E., 1976. The Hydrolysis of Cations. John Wiley & Sons.

Bennett, W.W., Lombi, E., Burton, E.D., Johnston, S.G., Kappen, P., Howard, D.L., Canfield, D.E., 2018. Synchrotron X-ray spectroscopy for investigating vanadium speciation in marine sediment: limitations and opportunities. J. Anal. At. Spectrom. 33, 1689–1699. https://doi.org/10.1039/c8ja00231b

Besnardiere, J., Petrissans, X., Ribot, F., Briois, V., Surcin, C., Morcrette, M., Buissette, V., Le Mercier, T., Cassaignon, S., Portehault, D., 2016. Nanoparticles of Low-Valence Vanadium Oxyhydroxides: Reaction Mechanisms and Polymorphism Control by Low-Temperature Aqueous Chemistry. Inorg. Chem. 55, 11502–11512. https://doi.org/10.1021/acs.inorgchem.6b02059

Bibi, I., Niazi, N.K., Choppala, G., Burton, E.D., 2018. Chromium(VI) removal by siderite ($FeCO_3$) in anoxic aqueous solutions: An X-ray absorption spectroscopy investigation. Sci. Total Environ. 640–641, 1424–1431. https://doi.org/10.1016/j.scitotenv.2018.06.003

Blackmore, D.P.T., Ellis, J., Riley, P.J., 1996. Treatment of a vanadium-containing effluent by adsorption/coprecipitation with iron oxyhydroxide. J. Pergamon 30, 2512–2516. https://doi.org/10.1016/0043-1354(96)00080-2

Borch, T., Kretzschmar, R., Kappler, A., Van Cappellen, P., Matthew, G.-V., Voegelin, A.,

Campbell, K., 2010. Biogeochemical redox processes and their impact on contaminant Dynamics. Environ. Sci. Technol. 44, 15–23. https://doi.org/10.1021/es9026248

Bostick, B.C., Fendorf, S., 2003. Arsenite sorption on troilite (FeS) and pyrite (FeS_2). Geochim. Cosmochim. Acta 67, 909–921. https://doi.org/10.1016/S0016-7037(02)01170-5

Brinza, L., Benning, L.G., Statham, P.J., 2008. Adsorption studies of Mo and V onto ferrihydrite. Mineral. Mag. 72, 385–388. https://doi.org/10.1180/minmag.2008.072.1.385

Brinza, L., Vu, H.P., Neamtu, M., Benning, L.G., 2019. Experimental and simulation results of the adsorption of Mo and V onto ferrihydrite. Sci. Rep. 9, 1365. https://doi.org/10.1038/s41598-018-37875-y

Brinza, L., Vu, H.P., Shaw, S., Mosselmans, J.F.W., Benning, L.G., 2015. Effect of Mo and V on the Hydrothermal Crystallization of Hematite from Ferrihydrite: An in Situ Energy Dispersive X-ray Diffraction and X-ray Absorption Spectroscopy Study. Cryst. Growth Des. 15, 4768–4780. https://doi.org/10.1021/acs.cgd.5b00173

Burke, I.T., Mayes, W.M., Peacock, C.L., Brown, A.P., Jarvis, A.P., Gruiz, K., 2012. Speciation of arsenic, chromium, and vanadium in red mud samples from the Ajka spill site, Hungary. Environ. Sci. Technol. 46, 3085–3092. https://doi.org/10.1021/es3003475

Canadian Council of Ministers of the Environment, 1999. Canadian Soil Quality Guidelines for the Protection of Environmental and Human Health: Vanadium (1997). Canadian Environmental Quality Guidelines, 1999, Canadian Council of Ministers of the Environment, Winnipeg. https://doi.org/10.1371/journal.pntd.0001325

Cannon, H.L., 1952. The effect of uranium-vanadium deposists on the vegetation of the Colorado Plateau. Am. Chem. Soc. Omega 250, 735–770. https://doi.org/10.2475/ajs.250.10.735

Carpentier, W., Sandra, K., De Smet, I., Brigé, A., De Smet, L., Van Beeumen, J., 2003. Microbial reduction and precipitation of vanadium by Shewanella oneidensis. Appl. Environ. Microbiol. 69, 3636–3639. https://doi.org/10.1128/AEM.69.6.3636

Chaurand, P., Rose, J., Briois, V., Salome, M., Proux, O., Nassif, V., Olivi, L., Susini, J., Hazemann, J.L., Bottero, J.Y., 2007. New methodological approach for the vanadium K-edge X-ray absorption near-edge structure interpretation: Application to the speciation of vanadium in oxide phases from steel slag. J. Phys. Chem. B 111, 5101–5110. https://doi.org/10.1021/jp063186i

Chen, G., Liu, H., 2017. Understanding the Reduction Kinetics of Aqueous Vanadium(V) and Transformation Products Using Rotating Ring-Disk Electrodes. Environ. Sci. Technol. 51, 11643–11651. https://doi.org/10.1021/acs.est.7b02021

Chen, M., Zhang, Y., Zheng, J., Liu, Y., Gao, Z., Yu, Z., Meng, C., 2018. PVP-assisted hydrothermal synthesis of $VO(OH)_2$ nanorods for supercapacitor electrode with excellent pseudocapacitance. Mater. Lett. 227, 217–220. https://doi.org/10.1016/j.matlet.2018.05.086

Christl, I., Brechbühl, Y., Graf, M., Kretzschmar, R., 2012. Polymerization of silicate on hematite surfaces and its influence on arsenic sorption. Environ. Sci. Technol. 46, 13235–13243. https://doi.org/10.1021/es303297m

Cook, O.A., 1947. High-Temperature Heat Contents of Vanadium Oxides. J. Am. Chem. Soc. 69, 331–333. https://doi.org/10.1021/ja01194a051

Cooper, M.A., Hawthorne, F.C., Grice, J.D., Haynes, P., 2003. Anorthominasragrite, $V^{4+}O(SO_4)(H_2O)_5$, a new mineral species from Temple Mountain, Emery County, Utah, U.S.A.: Description crystal structure and hydrogen bonding. Can. Mineral. 41, 959–979. https://doi.org/10.2113/gscanmin.41.4.959

Cornell, R.M., Schwertmann, U., 2003. The Iron Oxides: Structure, Properties, Reactions, Occurences and Uses. Wiley-VCH, Weinheim.

Couture, R., Rose, J., Kumar, N., Mitchell, K., Wallschla, D., Van Cappellen, P., 2013. Sorption of Arsenite, Arsenate, and Thioarsenates to Iron Oxides and Iron Sulfides: A Kinetic and Spectroscopic Investigation. Environ. Sci. Technol. 47, 5652–5659. https://doi.org/10.1021/es3049724

Crans, D.C., Smee, J.J., Gaidamauskas, E., Yang, L., 2004. The Chemistry and Biochemistry of Vanadium and the Biological Activities Exerted by Vanadium Compounds. Chem. Rev. 104, 849–902. https://doi.org/10.1021/cr020607t

Crans, D.C., Zhang, B., Gaidamauskas, E., Keramidas, A.D., Willsky, G.R., Roberts, C.R., 2010. Is vanadate reduced by thiols under biological conditions? Changing the Redox potential of V(V)/V(IV) by complexation in aqueous solution. Inorg. Chem. 49, 4245–4256. https://doi.org/10.1021/ic100080k

Cruywagen, J.J., 1999. Protonation, oligomerization, and condensation reaction of vanadate(V), molybdate(VI), and tungstate(VI). Adv. Inorg. Chem. 49, 127–182. https://doi.org/10.1016/S0898-8838(08)60270-6

Cruywagen, J.J., Heyns, J.B.B., Westra, A.N., 1996. Protonation Equilibria of Mononuclear Vanadate: Thermodynamic Evidence for the Expansion of the Coordination Number in VO^{2+}. Inorg. Chem. 35, 1556–1559. https://doi.org/10.1021/ic950832b

Das, S., Hendry, M.J., Essilfie-dughan, J., 2013. Adsorption of selenate onto ferrihydrite, goethite, and lepidocrocite under neutral pH conditions. Appl. Geochemistry 28, 185–193. https://doi.org/10.1016/j.apgeochem.2012.10.026

Davantès, A., Costa, D., Lefèvre, G., 2016. Molybdenum(VI) Adsorption onto Lepidocrocite (γ-FeOOH): In Situ Vibrational Spectroscopy and DFT+U Theoretical Study. J. Phys. Chem. C 120, 11871–11881. https://doi.org/10.1021/acs.jpcc.6b00722

Davantès, A., Costa, D., Lefèvre, G., 2015. Infrared Study of (Poly)tungstate Ions in Solution and Sorbed into Layered Double Hydroxides: Vibrational Calculations and In Situ Analysis. J. Phys. Chem. C 119, 12356–12364. https://doi.org/10.1021/acs.jpcc.5b01578

Davantes, A., Costa, D., Sallman, B., Rakshit, S., Lefevre, G., 2017. Surface polymerization of Mo(VI) and W(VI) anions on hematite revealed by in situ infrared spectroscopy and DFT+U theoretical study. J. Phys. Chem. C 121, 324–332. https://doi.org/10.1021/acs.jpcc.6b09721

Davantès, A., Lefèvre, G., 2016. Molecular orientation of molybdate ions adsorbed on goethite nanoparticles revealed by polarized in situ ATR-IR spectroscopy. Surf. Sci. 653, 88–91. https://doi.org/10.1016/j.susc.2016.06.007

Davantès, A., Lefèvre, G., 2015. In situ characterization of (poly)molybdate and (poly)tungstate ions sorbed onto iron (hydr)oxides by ATR-FTIR spectroscopy. Eur. Phys. J. Spec. Top. 224, 1977–1983. https://doi.org/10.1140/epjst/e2015-02514-8

Davantès, A., Lefèvre, G., 2013. In situ real time infrared spectroscopy of sorption of (poly)molybdate ions into layered double hydroxides. J. Phys. Chem. A 117, 12922–12929. https://doi.org/10.1021/jp408885k

Dixit, S., Hering, J.G., 2003. Comparison of Arsenic(V) and Arsenic(III) Sorption onto Iron Oxide Minerals: Implications for Arsenic Mobility. Environ. Sci. Technol. 37, 4182–4189. https://doi.org/10.1021/es030309t

Elvingson, K., González Baró, A., Pettersson, L., 1996. Speciation in vanadium bioinorganic systems. 2. An NMR, ESR, and potentiometric study of the aqueous H^+-vanadate-maltol system. Inorg. Chem. 35, 3388–3393. https://doi.org/10.1021/ic951195s

Environment and Climate Change Canada, 2016. Canadian Environmental Protection Act (1999). Federal Environmental Quality Guidelines: Vanadium [WWW Document]. URL http://www.ec.gc.ca/ese-ees/default.asp?lang=En&n=48D3A655-1

Farquhar, M.L., Charnock, J.M., Livens, F.R., Vaughan, D.J., 2002. Mechanisms of Arsenic Uptake from Aqueous Solution by Interaction with Goethite, Lepidocrocite, Mackinawite, and Pyrite: An X-ray Absorption Spectroscopy Study. Environ. Sci. Technol. 36, 1757–1762. https://doi.org/10.1021/es010216g

Finck, N., Dardenne, K., Bosbach, D., Geckeis, H., 2012. Selenide retention by mackinawite. Environ. Sci. Technol. 46, 10004–10011. https://doi.org/10.1021/es301878y

Gehring, A.U., Fry, I. V., Luster, J., Sposito, G., 1993. The chemical form of vanadium(IV) in kaolinite. Clays Clay Miner. 41, 662–667. https://doi.org/10.1346/CCMN.1993.0410604

Griffith, W.P., 1967. Vibrational Spectra of Metaphosphates, Meta-arsenates, and Metavanadates. J. Chem. Soc. A Inorganic, Phys. Theor. 905–908. https://doi.org/10.1039/J19670000905

Griffith, W.P., Lesniak, P.J.B., 1969. Raman Studies on Species in Aqueous Solutions. Part III. Vanadates, Molybdates, and Tungstates. J. Chem. Soc. A Inorganic, Phys. Theor. 1066–1071. https://doi.org/10.1039/J19690001066

Griffith, W.P., Wickins, T.D., 1966. Raman Studies on Species in Aqueous Solutions. Part I. The Vanadates. J. Chem. Soc. A Inorganic, Phys. Theor. 0, 1087–1090. https://doi.org/10.1039/J19660001087

Gückel, K., Tsushima, S., Foerstendorf, H., 2013. Structural characterization of the aqueous dimeric uranium(VI) species: $(UO_2)_2CO_3(OH)^{3-}$. Dalt. Trans. 42, 10172–10178. https://doi.org/10.1039/c3dt50814e

Guo, H., Ren, Y., Liu, Q., Zhao, K., Li, Y., 2013. Enhancement of arsenic adsorption during mineral transformation from siderite to goethite: Mechanism and application. Environ. Sci. Technol. 47, 1009–1016. https://doi.org/10.1021/es303503m

Gustafsson, J.P., 2019. Vanadium geochemistry in the biogeosphere –speciation, solid-solution interactions, and ecotoxicity. Appl. Geochemistry 102, 1–25. https://doi.org/10.1016/j.apgeochem.2018.12.027

Gustafsson, J.P., 2018. Visual MINTEQ version.3.1. https://vminteq.lwr.kth.se/

Han, D.S., Batchelor, B., Abdel-Wahab, A., 2011. Sorption of selenium(IV) and selenium(VI) to mackinawite (FeS): Effect of contact time, extent of removal, sorption envelopes. J. Hazard. Mater. 186, 451–457. https://doi.org/10.1016/j.jhazmat.2010.11.017

Hobson, A.J., Stewart, D.I., Bray, A.W., Mortimer, R.J.G., Mayes, W.M., Riley, A.L., Rogerson, M., Burke, I.T., 2018. Behaviour and fate of vanadium during the aerobic neutralisation of hyperalkaline slag leachate. Sci. Total Environ. 643, 1191–1199. https://doi.org/10.1016/j.scitotenv.2018.06.272

Hu, S., Yan, W., Duan, J., 2015. Polymerization of silicate on TiO_2 and its influence on arsenate adsorption: An ATR-FTIR study. Colloids Surfaces A Physicochem. Eng. Asp. 469, 180–186. https://doi.org/10.1016/j.colsurfa.2015.01.021

Hu, X., Yue, Y., Peng, X., 2018. Release kinetics of vanadium from vanadium (III, IV and V) oxides: Effect of pH, temperature and oxide dose. J. Environ. Sci. (China) 67, 96–103. https://doi.org/10.1016/j.jes.2017.08.006

Huang, J.H., Huang, F., Evans, L., Glasauer, S., 2015. Vanadium: Global (bio)geochemistry. Chem. Geol. 417, 68–89. https://doi.org/10.1016/j.chemgeo.2015.09.019

Hudson-Edwards, K.A., Byrne, P., Bird, G., Brewer, P.A., Burke, I.T., Jamieson, H.E., MacKlin, M.G., Williams, R.D., 2019. Origin and Fate of Vanadium in the Hazeltine Creek Catchment following the 2014 Mount Polley Mine Tailings Spill in British Columbia, Canada. Environ. Sci. Technol. 53, 4088–4098. https://doi.org/10.1021/acs.est.8b06391

Hug, S.J., 1997. In situ fourier transform infrared measurements of sulfate adsorption on hematite in aqueous solutions. J. Colloid Interface Sci. 188, 415–422. https://doi.org/10.1006/jcis.1996.4755

Hurlbut, C.S., Klein, C., 1977. Manual of Mineralogy. John Wiley & Sons.

Ikogou, M., Ona-Nguema, G., Juillot, F., Le Pape, P., Menguy, N., Richeux, N., Guigner, J.M., Noël, V., Brest, J., Baptiste, B., Morin, G., 2017. Long-term sequestration of nickel in mackinawite formed by Desulfovibrio capillatus upon Fe(III)-citrate reduction in the presence of thiosulfate. Appl. Geochemistry 80, 143–154. https://doi.org/10.1016/j.apgeochem.2017.02.019

Jeong, Y., Maohong, F., Van Leeuwen, J., Belczyk, J.F., 2007. Effect of competing solutes on arsenic(V) adsorption using iron and aluminum oxides. J. Environ. Sci. 19, 910–919. https://doi.org/10.1016/S1001-0742(07)60151-X

Johnston, S.G., Burton, E.D., Aaso, T., Tuckerman, G., 2014. Sulfur, iron and carbon cycling following hydrological restoration of acidic freshwater wetlands. Chem. Geol. 371, 9–26. https://doi.org/10.1016/j.chemgeo.2014.02.001

Jönsson, J., Sherman, D.M., 2008. Sorption of As(III) and As(V) to siderite, green rust (fougerite) and magnetite: Implications for arsenic release in anoxic groundwaters. Chem. Geol. 255, 173–181. https://doi.org/10.1016/j.chemgeo.2008.06.036

Kaur, N., Singh, B., Kennedy, B.J., Gräfe, M., 2009. The preparation and characterization of vanadium-substituted goethite: The importance of temperature. Geochim. Cosmochim. Acta 73, 582–593. https://doi.org/10.1016/j.gca.2008.10.025

Krakowiak, J., Lundberg, D., Persson, I., 2012. A coordination chemistry study of hydrated and solvated cationic vanadium ions in oxidation states +III, +IV, and +V in solution and solid state. Inorg. Chem. 51, 9598–9609. https://doi.org/10.1021/ic300202f

Larson, J.W., 1995. Thermochemistry of Vanadium(5+) in Aqueous Solutions. J. Chem. Eng. Data 40, 1276–1280. https://doi.org/10.1021/je00022a030

Larsson, M.A., Baken, S., Gustafsson, J.P., Hadialhejazi, G., Smolders, E., 2013. Vanadium bioavailability and toxicity to soil microorganisms and plants. Environ. Toxicol. Chem. 32, 2266–2273. https://doi.org/10.1002/etc.2322

Larsson, M.A., Persson, A.I., Sjo, B.C., Gustafsson, J.P., 2017. Vanadate complexation to ferrihydrite : X-ray absorption spectroscopy and CD-MUSIC modelling. Environ. Chem. 14, 141–150. https://doi.org/10.1071/EN16174

Lefèvre, G., Noinville, S., Fédoroff, M., 2006. Study of uranyl sorption onto hematite by in situ attenuated total reflection-infrared spectroscopy. J. Colloid Interface Sci. 296, 608–613. https://doi.org/10.1016/j.jcis.2005.09.016

Levina, A., McLeod, A.I., Lay, P.A., 2014. Vanadium speciation by XANES spectroscopy: A three-dimensional approach. Chem. - A Eur. J. 20, 12056–12060. https://doi.org/10.1002/chem.201403993

Lewan, M.D., 1984. Factors controlling the proportionality of vanadium to nickel in crude oils. Geochim. Cosmochim. Acta 48, 2231–2238. https://doi.org/10.1016/0016-7037(84)90219-9

Li, X.S., Le, X.C., 2007. Speciation of vanadium in oilsand coke and bacterial culture by high performance liquid chromatography inductively coupled plasma mass spectrometry. Anal. Chim. Acta 602, 17–22. https://doi.org/10.1016/j.aca.2007.09.004

López, L., Monaco, S. Lo, Volkman, J.K., 2015. Evidence for mixed and biodegraded crude oils in the Socororo field, Eastern Venezuela Basin. Org. Geochem. 82, 12–21. https://doi.org/10.1016/j.orggeochem.2015.02.006

Ma, B., Kang, M., Zheng, Z., Chen, F., Xie, J., Charlet, L., Liu, C., 2014. The reductive immobilization of aqueous Se(IV) by natural pyrrhotite. J. Hazard. Mater. 276, 422–432. https://doi.org/10.1016/j.jhazmat.2014.05.066

Manceau, A., 1995. The mechanism of anion adsorption on iron oxides: Evidence for the bonding of arsenate tetrahedra on free $Fe(O,OH)_6$ edges. Geochim. Cosmochim. Acta 59, 3647–3653. https://doi.org/10.1016/0016-7037(95)00275-5

Manning, B.A., Hunt, M.L., Amrhein, C., Yarmoff, J.A., 2002. Arsenic(III) and arsenic(V) reactions with zerovalent iron corrosion products. Environ. Sci. Technol. 36, 5455–5461. https://doi.org/10.1021/es0206846

Mayes, W.M., Jarvis, A.P., Burke, I.T., Walton, M., Feigl, V., Klebercz, O., Gruiz, K., 2011. Dispersal and attenuation of trace contaminants downstream of the Ajka bauxite residue (Red Mud) depository failure, Hungary. Environ. Sci. Technol. 45, 5147–5155. https://doi.org/10.1021/es200850y

Mayordomo, N., Foerstendorf, H., Lützenkirchen, J., Heim, K., Weiss, S., Alonso, U., Missana, T., Schmeide, K., Jordan, N., 2018. Selenium(IV) Sorption onto γ-Al_2O_3 : A Consistent Description of the Surface Speciation by Spectroscopy and Thermodynamic Modeling. Environ. Sci. Technol. 52, 581–588. https://doi.org/10.1021/acs.est.7b04546

Mitchell, K., Couture, R.-M., Johnson, T.M., Mason, P.R.D., Van Cappellen, P., 2013. Selenium sorption and isotope fractionation: Iron(III) oxides versus iron (II) sulfides. Chem. Geol. 342, 21–28. https://doi.org/10.1016/j.chemgeo.2013.01.017

Morse, J.W., Arakaki, T., 1993. Adsorption and coprecipitation of divalent metals with mackinawite (FeS). Geochim. Cosmochim. Acta 57, 3635–3640. https://doi.org/10.1016/0016-7037(93)90145-M

Morse, J.W., Cornwell, J.C., 1987. Analysis and distribution of iron sulfide minerals in recent anoxic marine sediemts. Mar. Chem. 22, 55–69. https://doi.org/10.1016/0304-4203(87)90048-X

Moskalyk, R.R., Alfantazi, A.M., 2003. Processing of vanadium: A review. Miner. Eng. 16, 793–805. https://doi.org/10.1016/S0892-6875(03)00213-9

Motschi, H., Rudin, M., 1984. Al-27 ENDOR study of VO_2^+ adsorbed on delta-alumina. Colloid Polym. Sci. 262, 579–583. https://doi.org/10.1007/BF01451522

Myneni, S.C.B., Tokunaga, T.K., Brown Jr., G.E., 1997. Abiotic Selenium Redox Transformations in the Presence of Fe(II,III) Oxides. Science (80). 278, 1106–1109.

Myneni, S.C.B., Traina, S.J., Waychunas, G.A., Logan, T.J., 1998. Experimental and theoretical vibrational spectroscopic evaluation of arsenate coordination in aqueous solutions, solids, and at mineral-water interfaces. Geochim. Cosmochim. Acta 62, 3285–3300. https://doi.org/10.1016/S0016-7037(98)00222-1

Naeem, A., Westerhoff, P., Mustafa, S., 2007. Vanadium removal by metal (hydr)oxide adsorbents. Water Res. 41, 1596–1602. https://doi.org/10.1016/j.watres.2007.01.002

Nakamoto, K., 1997. Infrared and Raman Spectra of Inorganic and Coordination Compounds, Part B, 5th Editio. ed. Wiley-Interscience, New York.

Nesbitt, J.A., 2016. Geochemical investigation of fluid petroleum coke deposits at an oil sands mine in Northern Alberta, Canada.

Nesbitt, J.A., Lindsay, M.B.J., 2017. Vanadium Geochemistry of Oil Sands Fluid Petroleum Coke. Environ. Sci. Technol. 51, 3102–3109. https://doi.org/10.1021/acs.est.6b05682

Nesbitt, J.A., Lindsay, M.B.J., Chen, N., 2017. Geochemical characteristics of oil sands fluid petroleum coke. Appl. Geochemistry 76, 148–158. https://doi.org/10.1016/j.apgeochem.2016.11.023

Ortiz-bernad, I., Anderson, R.T., Vrionis, H.A., Lovley, D.R., Ortiz-bernad, I., Anderson, R.T., Vrionis, H.A., Lovley, D.R., 2004. Vanadium Respiration by Geobacter metallireducens: Novel Strategy for In Situ Removal of Vanadium from Groundwater. Appl. Environ. Microbiol. 70, 3091–3095. https://doi.org/10.1128/AEM.70.5.3091

Parkhurst, D.L., Appelo, C.A.J., 2013. Description of input and examples for PHREEQC version 3: a computer program for speciation, batch-reaction, one-dimensional transport, and inverse geochemical calculations. Tech. Methods 6-A43. U.S. Geol. Surv. Denver, USA.

Peacock, C.L., Sherman, D.M., 2004. Vanadium(V) adsorption onto goethite (α-FeOOH) at pH 1.5 to 12: A surface complexation model based on ab initio molecular geometries and EXAFS spectroscopy. Geochim. Cosmochim. Acta 68, 1723–1733. https://doi.org/10.1016/j.gca.2003.10.018

Peak, D., Ford, R.G., Sparks, D.L., 1999. An in Situ ATR-FTIR Investigation of Sulfate Bonding Mechanisms on Goethite. J. Colloid Interface Sci. 218, 289–299.

Peak, D., Luther, G.W.I., Sparks, D., 2003. ATR-FTIR spectroscopic studies of boric acid adsorption on hydrous ferric oxide. Geochim. Cosmochim. Acta 67, 2551–2560. https://doi.org/10.1016/S0016-7037(03)00096-6

Phillips, D.H., Watson, D.B., Roh, Y., Gu, B., 2003. Mineralogical characteristics and transformations during long-term operation of a zerovalent iron reactive barrier. J. Environ. Qual. 32, 2033–2045. https://doi.org/10.2134/jeq2003.2033

Prathap, K., Namasivayam, C., 2010. Adsorption of vanadate(V) on Fe(III)/Cr(III) hydroxide waste. Environ. Chem. Lett. 8, 363–371. https://doi.org/10.1007/s10311-009-0234-x

Puttaswamy, N., Liber, K., 2011. Identifying the causes of oil sands coke leachate toxicity to aquatic invertebrates. Environ. Toxicol. Chem. 30, 2576–2585. https://doi.org/10.1002/etc.653

Puttaswamy, N., Turcotte, D., Liber, K., 2010. Variation in toxicity response of Ceriodaphnia dubia to Athabasca oil sands coke leachates. Chemosphere 80, 489–497. https://doi.org/10.1016/j.chemosphere.2010.04.071

Qu, X.-F., Yao, Q.-Z., Zhou, G.-T., 2011. Synthesis of siderite microspheres and their transformation to magnetite microspheres. Eur. J. Mineral. 23, 759–770. https://doi.org/10.1127/0935-1221/2011/0023-2134

Ravel, B., Newville, M., 2005. ATHENA, ARTEMIS, HEPHAESTUS: Data analysis for X-ray absorption spectroscopy using IFEFFIT. J. Synchrotron Radiat. 12, 537–541. https://doi.org/10.1107/S0909049505012719

Rehder, D., 2015. The role of vanadium in biology. Metallomics 7, 730–742. https://doi.org/10.1039/c4mt00304g

Rehder, D., 1991. The Bioinorganic Chemistry of Vanadium. Chem. Br. 30, 148–167.

Reijonen, I., Metzler, M., Hartikainen, H., 2016. Impact of soil pH and organic matter on the chemical bioavailability of vanadium species: The underlying basis for risk assessment. Environ. Pollut. 210, 371–379. https://doi.org/10.1016/j.envpol.2015.12.046

Rickard, D., Luther, G.W.I., 2007. Chemistry of Iron Sulfides. Chem. Rev. 107, 514–562. https://doi.org/10.1021/cr0503658

RIVM Letter Report 601714021/2012; National Institute for Public Health and the Environment, B., 2012. Environmental Risk Limits for Vanadium in Water: A Proposal for Water Quality Standards in Accordance with the Water Framework Directive.

Roddick-Lanzilotta, A.J., McQuillan, A.J., Craw, D., 2002. Infrared spectroscopic characterisation of arsenate(V) ion adsorption from mine waters, Macraes mine, New Zealand. Appl. Geochemistry 17, 445–454. https://doi.org/10.1016/S0883-2927(01)00116-0

Salak, A.N., Tedim, J., Kuznetsova, A.I., Ribeiro, J.L., Vieira, L.G., Zheludkevich, M.L., Ferreira, M.G.S., 2012. Comparative X-ray diffraction and infrared spectroscopy study of Zn-Al layered double hydroxides: Vanadate vs nitrate. Chem. Phys. 397, 102–108. https://doi.org/10.1016/j.chemphys.2012.01.026

Scheinost, A.C., Charlet, L., 2008. Selenite Reduction by Mackinawite, Magnetite and Siderite: XAS Characterization of Nanosized Redox Products. Environ. Sci. Technol. 42, 1984–1989. https://doi.org/10.1021/es071573f

Schiffer, S., Liber, K., 2017. Estimation of vanadium water quality benchmarks for the protection of aquatic life with relevance to the Athabasca Oil Sands region using species sensitivity distributions. Environ. Toxicol. Chem. 36, 3034–3044. https://doi.org/10.1002/etc.3871

Schlesinger, W.H., Klein, E.M., Vengosh, A., 2017. Global biogeochemical cycle of vanadium. Proc. Natl. Acad. Sci. 114, E11092–E11100. https://doi.org/10.1073/pnas.1715500114

Schwertmann, U., Pfab, G., 1994. Structural vanadium in synthetic goethite. Geochim. Cosmochim. Acta 58, 4349–4352. https://doi.org/10.1016/0016-7037(94)90338-7

Seargeant, L.E., Stinson, R.A., 1979. Inhibition of human alkaline phosphatases by vanadate. Biochem. J. 181, 247–50. https://doi.org/10.1042/bj1810247

Shaheen, S.M., Alessi, D.S., Tack, F.M.G., Ok, Y.S., Kim, K.H., Gustafsson, J.P., Sparks, D.L., Rinklebe, J., 2019. Redox chemistry of vanadium in soils and sediments: Interactions with colloidal materials, mobilization, speciation, and relevant environmental implications - A review. Adv. Colloid Interface Sci. 265, 1–13. https://doi.org/10.1016/j.cis.2019.01.002

Shiller, A.M., Boyle, E.A., 1987. Dissolved vanadium in rivers and estuaries. Earth Planet. Sci. Lett. 86, 214–224. https://doi.org/10.1016/0012-821X(87)90222-6

Sia, S.-G., Abdullah, W.H., 2011. Concentration and association of minor and trace elements in Mukah coal from Sarawak , Malaysia , with emphasis on the potentially hazardous trace elements. Int. J. Coal Geol. 88, 179–193. https://doi.org/10.1016/j.coal.2011.09.011

Sigg, L., Stumm, W., 1980. The interaction of anions and weak acids with the hydrous goethite (α-FeOOH) surface. Colloids and Surfaces 2, 101–117. https://doi.org/10.1016/0166-6622(81)80001-7

Spadini, L., Bott, M., Wehrli, B., Manceau, A., 2003. Analysis of the Major Fe Bearing Mineral Phases in Recent Lake Sediments by EXAFS Spectroscopy. Aquat. Geochemistry 9, 1–17. https://doi.org/10.1023/B:AQUA.0000005608.69468.1e

Sun, J., Bostick, B.C., 2015. Effects of tungstate polymerization on tungsten(VI) adsorption on ferrihydrite. Chem. Geol. 417, 21–31. https://doi.org/10.1016/j.chemgeo.2015.09.015

Swedlund, P.J., Miskelly, G.M., McQuillan, A.J., 2010. Silicic acid adsorption and oligomerization at the ferrihydrite - Water interface: Interpretation of ATR-IR spectra based on a model surface structure. Langmuir 26, 3394–3401. https://doi.org/10.1021/la903160q

Toby, B.H., Von Dreele, R.B., 2013. GSAS-II: The genesis of a modern open-source all purpose crystallography software package. J. Appl. Crystallogr. 46, 544–549. https://doi.org/10.1107/S0021889813003531

Tribovillard, N., Algeo, T.J., Lyons, T., Riboulleau, A., 2006. Trace metals as paleoredox and paleoproductivity proxies: An update. Chem. Geol. 232, 12–32. https://doi.org/10.1016/j.chemgeo.2006.02.012

Twu, J., Dutta, P.K., 1990. Decavanadate ion-pillared hydrotalcite: spectroscopic studies of the thermal decomposition process. J. Catal. 124, 503–510. https://doi.org/10.1016/0021-9517(90)90196-Q

Twu, J., Dutta, P.K., 1989. Structure and reactivity of oxovanadate anions in layered lithium aluminate materials. J. Phys. Chem. 93, 7863–7868. https://doi.org/10.1021/j100360a028

USEPA, 2016. US Environmental Protection Agency Drinking Water Contaminant Candidate List 4 (CCL4). https://www.epa.gov/ccl/chemical-contaminants-ccl-4

Wang, X., Wang, Z., Peak, D., Tang, Y., Feng, X., Zhu, M., 2018. Quantification of Coexisting Inner- and Outer-Sphere Complexation of Sulfate on Hematite Surfaces. ACS Earth Sp. Chem. 2, 387–398. https://doi.org/10.1021/acsearthspacechem.7b00154

Wang, Z., Ma, T., Zhu, Y., Abass, O.K., Liu, L., Su, C., Shan, H., 2018. Application of siderite tailings in water-supply well for As removal: Experiments and field tests. Int. Biodeterior. Biodegradation 128, 85–93. https://doi.org/10.1016/j.ibiod.2016.10.029

Wanty, R.B., Goldhaber, M.B., 1992. Thermodynamics and Kinetics of Reactions Involving Vanadium in Natural Systems : Accumulation of Vanadium in Sedimentary-Rocks. Geochim. Cosmochim. Acta 56, 1471–1483. https://doi.org/10.1016/0016-7037(92)90217-7

Watt, J.A.J., Burke, I.T., Edwards, R.A., Malcolm, H.M., Mayes, W.M., Olszewska, J.P., Pan, G., Graham, M.C., Heal, K. V., Rose, N.L., Turner, S.D., Spears, B.M., 2018. Vanadium: A Re-Emerging Environmental Hazard. Environ. Sci. Technol. 52, 11973–11974. https://doi.org/10.1021/acs.est.8b05560

Wehrli, B., Stumm, W., 1989. Vanadyl in natural waters: Adsorption and hydrolysis promote oxygenation. Geochim. Cosmochim. Acta 53, 69–77. https://doi.org/10.1016/0016-7037(89)90273-1

Wehrli, B., Stumm, W., 1988. Oxygenation of Vanadyl(IV): Effect of coordinated surface hydroxyl groups and OH-. Langmuir 4, 753–758. https://doi.org/10.1021/la00081a045

Wen, B., Wang, Q., Lin, Y., Chernova, N.A., Karki, K., Chung, Y., Omenya, F., Sallis, S., Piper, L.F.J., Ong, S.P., Whittingham, M.S., 2016. Molybdenum Substituted Vanadyl Phosphate ϵ-$VOPO_4$ with Enhanced Two-Electron Transfer Reversibility and Kinetics for Lithium-Ion Batteries. Chem. Mater. 28, 3159–3170. https://doi.org/10.1021/acs.chemmater.6b00891

Wen, J., Ning, P., Cao, H., Zhao, H., Sun, Z., Zhang, Y., 2019. Novel method for characterization of aqueous vanadium species: A perspective for the transition metal chemical speciation studies. J. Hazard. Mater. 364, 91–99. https://doi.org/10.1016/j.jhazmat.2018.09.069

White, A.F., Peterson, M.L., 1996. Reduction of aqueous transition metal species on the surfaces of Fe(II)-containing oxides. Geochim. Cosmochim. Acta 60, 3799–3814. https://doi.org/10.1016/0016-7037(96)00213-X

Wilkin, R.T., Beak, D.G., 2017. Uptake of nickel by synthetic mackinawite. Chem. Geol. 462, 15–29. https://doi.org/10.1016/j.chemgeo.2017.04.023

Wisawapipat, W., Kretzschmar, R., 2017. Solid Phase Speciation and Solubility of Vanadium in Highly Weathered Soils. Environ. Sci. Technol. 51, 8254–8262. https://doi.org/10.1021/acs.est.7b01005

Wolthers, M., Charlet, L., van Der Linde, P.R., Rickard, D., van Der Weijden, C.H., 2005a. Surface chemistry of disordered mackinawite (FeS). Geochim. Cosmochim. Acta 69, 3469–3481. https://doi.org/10.1016/j.gca.2005.01.027

Wolthers, M., Charlet, L., van Der Weijden, C.H., van Der Linde, P.R., Rickard, D., 2005b. Arsenic mobility in the ambient sulfidic environment: Sorption of arsenic(V) and arsenic(III) onto disordered mackinawite. Geochim. Cosmochim. Acta 69, 3483–3492. https://doi.org/10.1016/j.gca.2005.03.003

Wolthers, M., Van Der Gaast, S., Rickard, D., 2003. The structure of disordered mackinawite. Am. Mineral. 88, 2007–2015. https://doi.org/10.2138/am-2003-11-1245

Wright, M.T., Belitz, K., 2010. Factors controlling the regional distribution of vanadium in groundwater. Ground Water 48, 515–525. https://doi.org/10.1111/j.1745-6584.2009.00666.x

Wright, M.T., Stollenwerk, K.G., Belitz, K., 2014. Assessing the solubility controls on vanadium in groundwater, northeastern San Joaquin Valley, CA. Appl. Geochemistry 48, 41–52. https://doi.org/10.1016/j.apgeochem.2014.06.025

Yalcintas, E., Scheinost, A.C., Gaona, X., Altmaier, M., 2016. Systematic XAS study on the reduction and uptake of Tc by magnetite and mackinawite. Dalt. Trans. 45, 17874–17885. https://doi.org/10.1039/c6dt02872a

Yang, J., Tang, Y., Yang, K., Rouff, A.A., Elzinga, E.J., Huang, J.H., 2014. Leaching characteristics of vanadium in mine tailings and soils near a vanadium titanomagnetite mining site. J. Hazard. Mater. 264, 498–504. https://doi.org/10.1016/j.jhazmat.2013.09.063

Yu, Y. qi, Yang, J. yan, 2019. Oral bioaccessibility and health risk assessment of vanadium(IV) and vanadium(V) in a vanadium titanomagnetite mining region by a whole digestive system in-vitro method (WDSM). Chemosphere 215, 294–304. https://doi.org/10.1016/j.chemosphere.2018.10.042

Zhang, H., Selim, H.M., 2005. Kinetics of Arsenate Adsorption−Desorption in Soils. Environ. Sci. Technol. 39, 6101–6108. https://doi.org/10.1021/es050334u

Zhu, H., Xiao, X., Guo, Z., Han, X., Liang, Y., Zhang, Y., Zhou, C., 2018. Adsorption of vanadium (V) on natural kaolinite and montmorillonite: Characteristics and mechanism. Appl. Clay Sci. 161, 310–316. https://doi.org/10.1016/j.clay.2018.04.035

Zubot, W., Mackinnon, M.D., Chelme-Ayala, P., Smith, D.W., El-Din, M.G., 2012. Petroleum

coke adsorption as a water management option for oil sands process-affected water. Sci. Total Environ. 427–428, 364–372. https://doi.org/10.1016/j.scitotenv.2012.04.024

Appendix A: Supplementary Information for Chapter 3

A.1. Material and Methods

A.1.1. Mineral synthesis

Synthesis of 2-line ferrihydrite, siderite, and mackinawite were modified from Cornell and Schwertmann (2003), Qu et al. (2011), and Wolthers et al. (2003), respectively. Ferrihydrite was synthesized by dissolving 40 g of $FeCl_3$ in 500 mL of DI water and titrated with 1.0 M KOH to pH 7 to 8 and stirred vigorously for 1 h (Cornell and Schwertmann, 2003). Siderite microspheres were prepared by dissolving ascorbic acid (0.20 M) in 30 mL of DI water followed by the addition of $FeSO_4 \cdot 7H_2O$ salt (0.067 M). This solution was then mixed with 30 mL of 0.20 M Na_2CO_3. Following 10 min of mixing a cloudy green-blue precipitate formed, at which point the mixture is transferred into a 100 mL sealable amber flask and heating to 130 °C for 4 hrs, and then allowed to cool to room temperature (Qu et al., 2011). Amorphous mackinawite was synthesized following a modified method of Wolthers et al. (2003), where 100 mL of $FeSO_4 \cdot 7H_2O$ and $Na_2S \cdot 9H_2O$ yielding concentrations of 0.6 M for Fe^{2+} and S^{2-}, respectively. These solutions were then mixed together, instantly precipitating black FeS particles, which is then covered in aluminum foil to prevent photooxidation and allowed to mix for 1 h. The V(IV) standard, $VO(OH)_2$, was synthesized by a modified method from Chen et al. (2018), whereby ~5.0 g of $VOSO_4$ is dissolved in 50 mL DI and titrated to pH 6.0 using 1.0 M NaOH. Following titration, a brown/gray precipitate formed and was allowed to settle for 2 hr prior to separation. All synthesis procedures were followed by rinsing with DI water to remove residual ions (i.e., SO_4^{2-}, Fe^{2+}, and S^{2-}) by centrifugation (4-5 times) or vacuum filtration. Following rinsing, the synthetic minerals were immediately freeze dried for at least 24 h and stored at −20 °C.

A.1.2. X-ray Diffraction

Synchrotron-based powder XRD was performed on the Canadian Macromolecular Crystallography Facility (08ID-1) at the Canadian Light Source (CLS), Saskatoon, Saskatchewan. Samples were prepared under anoxic conditions in an anaerobic chamber. Solids were finely ground in a mortar and pestle and transferred into polyimide capillary tubes (Cole-Palmer, Vermont Hills, Il, USA), sealed with glue (Loctite 454) to limit oxygen ingress into the sample and transported to the beam line in a vacuum container. The incident X-ray energy was 18 keV

(0.69 Å), and was selected using Si(111) double crystal monochromator. Scans were taken in triplicate (10 s per scan) at the maximum energy (18 keV) with the area detector set 250 mm from the sample holder. The software GSAS-II was used to calibrate the two dimensional diffraction images and integrate them into one dimension diffraction peak profiles (Toby and Von Dreele, 2013). Calibration of the scans was done using a lanthanum hexaboride (LaB_6) standard, with scans integrated from 5 to 100° 2Θ between the 90° and 270° azimuths. Mineral phase identification was performed on Match! (Version 3.7.0, Crystal Impact).

A.1.3. Raman Spectroscopy

Synthetic siderite, Fe (hydr)oxides, and Fe sulfides purity was confirmed by Raman spectroscopy at the Saskatchewan Structural Sciences Centre, University of Saskatchewan, Saskatoon, Saskatchewan. Scans were performed using a Renishaw InVia Raman microscope with a solid state laser diode operating at 514 nm with a 1800 lines mm^{-1} (633/780) grating at a laser power of <0.1%. The instrumental silicon calibration standard was measured at 520 cm^{-1}. Repeated scans (n = 30) were collected using the 50x objective over a range of 100 - 2000 cm^{-1}.

Table A.1. Properties of synthetic phases selected for V sorption experiments, including: ferrihydrite (Fh) and magnetite (Mag), pyrite (Py), mackinawite (Mck), and siderite (Sd). Specific surface area (SSA) was determined using the BET N2 sorption method, particle size was estimated from TEM images, and point of zero charge (pHPZC) values are referenced from literature.

Sample ID	SSA (m^2 g^{-1})	Particle Size (µm)	pH_{PZC}
Fh-avg	261.4 ± 1.1	0.01	7.5 – 8.0[1]
Mag-avg	11.1 ± 0.9	< 0.25	7.5 – 8.0[1]
Py-avg	1.1 ± 0.7	5 – 30	~3.0[2]
Mck-avg	17.8 ± 1.7	0.004	~7.5[3]
3-Sd-avg	11.7 ± 5.2	5 – 15	~6.0[4]
3-Sd-a	5.9		
3-Sd-b	10.2		
3-Sd-c	12.3		
3-Sd-d	18.4		
48-Sid	13.2		

[1]Cornell and Schwertmann (2003)

[2]Han et al. (2012)

[3]Wolthers et al. (2005)

[4]Charlet et al. (1990)

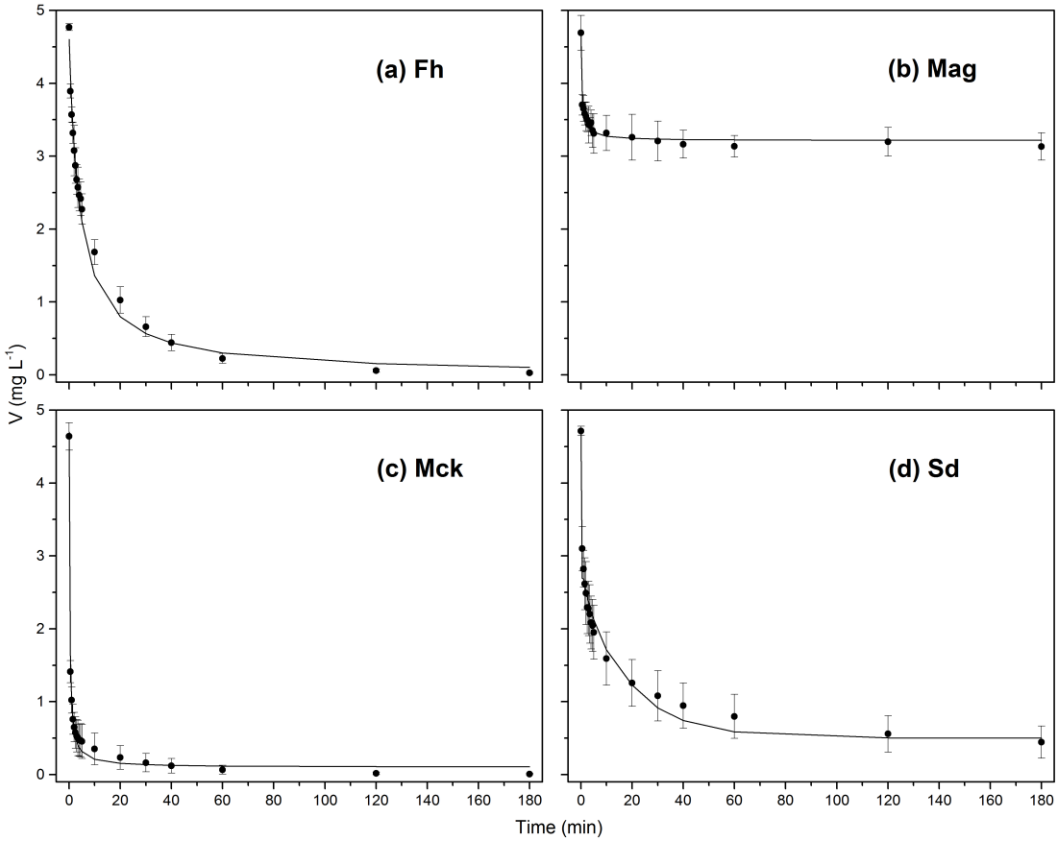

Figure A.1. Measured (closed circles) and kinetically modeled (solid lines) concentrations of V reacted with ferrihydrite (a), magnetite (b), mackinawite (c), siderite (d) at pH 7 in MOPS-buffered suspension (2 g L^{-1}).

Table A.2. Rate constants for averaged sorption data using standard kinetic models. Where $[V]_0$ is the initial V concentration, $[Fe]_0$ is the initial Fe concentration used only for modeling second order kinetic removal by siderite, k is the rate constant, and R^2 and RMSE values are goodness of fit parameters.

Experiment ID	Reaction Order	$[V]_0$ (mg L^{-1})	$[Fe]_0$ (mg L^{-1})	k	R^2	RMSE
3-Fh	Psuedo 1st	4.77	NA	0.052	0.989	0.145
3-Mag	Psuedo 1st	4.69	NA	1.579	0.961	0.067
3-Sd	Second	4.71	13.8	0.005	0.977	0.155
3-Mck	Psuedo 1st	4.64	NA	0.732	0.987	0.118

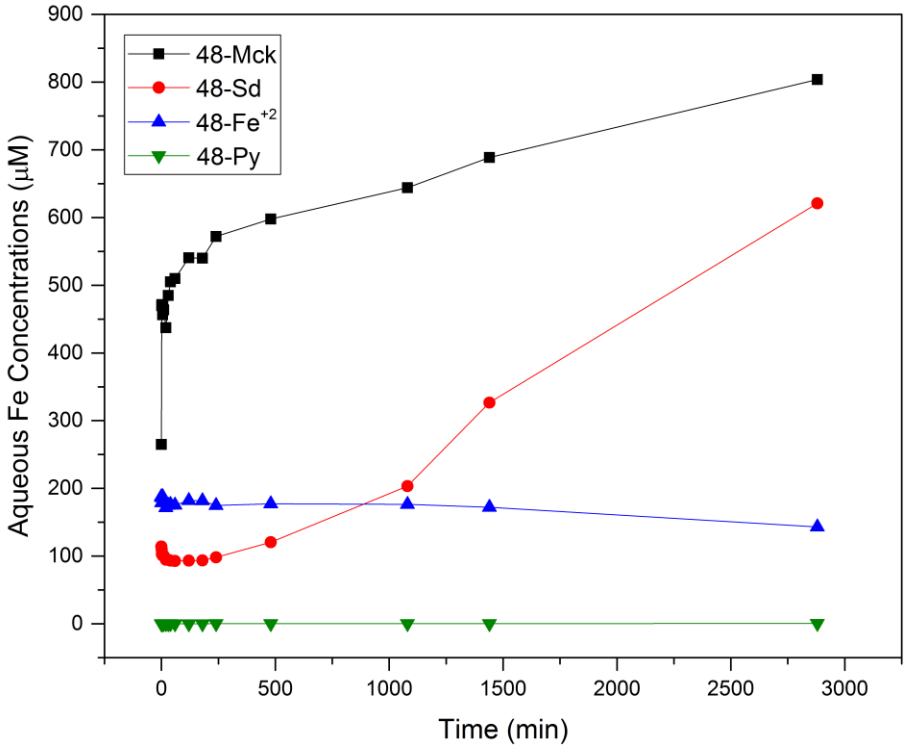

Figure A.2. Aqueous iron concentrations for reacted mackinawite (black squares), siderite (red circles), $Fe^{+2}_{(aq)}$ (blue triangles), and pyrite (green triangles) at pH 7 in MOPS-buffered suspension over 48 hours.

Table A.3. Summary of V K-edge XANES pre-edge peak analysis. The parameter $E_{1/2}$ refers to the energy on the main edge where the normalized intensity is equal to 0.5.

Solid Phase	Pre-edge peak				Main edge	Average Oxidation State
	Centroid (eV)	Position (eV)	Height	Area	$E_{1/2}$	
$Na_3V^{V}O_4$	5469.8	5469.8	0.89	1.75	5481.6	5.09
$V^{IV}O(OH)_2$	5469.4	5469.4	0.32	0.77	5478.4	3.95
$V^{IV}OSO_4$	5469.5	5469.6	0.31	0.71	5478.1	3.87
$V^{III}Cl_3$	5468.5	5468.1	0.02	0.05	5475.3	3.09
3-Fh	5469.9	5469.8	0.65	1.58	5481.8	4.89
48-Fh	5469.9	5470.1	0.66	1.60	5481.8	4.92
3-Mag	5469.8	5469.8	0.63	1.49	5481.3	4.79
48-Mag	5469.9	5470.1	0.63	1.50	5481.1	4.80
3-Sd-a	5469.8	5469.8	0.45	1.11	5480.1	4.35
3-Sd-b	5469.8	5469.8	0.43	1.08	5480.1	4.31
48-Sd	5469.8	5469.6	0.35	0.92	5479.9	4.12
3-Mck	5469.6	5469.6	0.28	0.65	5479.3	3.80
48-Mck	5469.6	5469.6	0.23	0.52	5479.1	3.64
48-Fe^{2+}	5469.7	5469.6	0.39	1.06	5479.4	4.29

Table A.4. EXAFS parameters from non-linear least squares shell-fit results for all reference compounds and sorption samples, where S_0^2 is amplitude function, ΔE is the energy-shift parameter, CN is coordination number, R refers to bond distance, σ^2 is the Debye-Waller factor, and χ^2_{red} is the reduced chi-squared.

Sample ID	k-range	S_0^2	ΔE	CN ±25%	R(Å)	σ^2(Å^2)	χ^2_{red}	R factor
$Na_3V^VO_4$								
V-O	3.5-10.3	0.89(9)	9(1)	4.0[a]	1.713(5)	0.0039(8)	180	0.060
V-O-O MS				12.0[a]	3.14(8)	0.007(3)		
$V^{IV}O(OH)_2$								
V-O				1.0[b]	1.614(5)	0.0006(5)		
V-O1				4.0[b]	2.000(7)	0.0079(6)		
V-O2	3.0-14.0	0.950(2)	8.3(4)	1.0[b]	2.527(9)	0.009(1)	45	0.040
V-V1				4.0[b]	3.04(2)	0.017(2)		
V-V2				4.0[b]	3.24(2)	0.015(2)		
V-V3				4.0[b]	3.43(2)	0.011(2)		
$V^{IV}OSO_4$								
V-O				1.0[c,d,e]	1.597(2)	0.0005(7)		
V-O1	3.0-14.0	1.06(7)	7(1)	4.0[c,d,e]	2.018(5)	0.0056(7)	60	0.050
V-O2				1.0[c,d,e]	2.52(6)	0.006(3)		
V-S				2.0[c,d,e]	3.27(4)	0.013(7)		
$V^{III}Cl_3$								
V-Cl1				1.0	2.03(2)	0.002(2)		
V-Cl2	2.0-10.3	0.94(3)	−7.8(7)	4.0	2.27(1)	0.005(2)	321	0.090
V-Cl3				1.0	2.41(5)	0.003(1)		
V-V				3.0	3.41(7)	0.014(2)		
V-Cl4				6.0	4.80(5)	0.011(7)		
3-Fh								
V-O				4.0[a]	1.711(9)	0.007(1)		
V-Fe1	2.5-10.5	0.94(1)	7.1(6)	1.0[a]	2.68(6)	0.0141(2)	615	0.105
V-O-O MS				12.0[a]	3.169(2)	0.007(2)		
V-Fe2				2.0[a]	3.32(7)	0.009(1)		
48-Fh								
V-O				4.0[a]	1.703(5)	0.006(1)		
V-Fe1	2.5-10.5	0.94(2)	6.4(7)	1.0[a]	2.66(5)	0.0123(5)	1100	0.108
V-O-O MS				12.0[a]	3.170(9)	0.007(2)		
V-Fe2				2.0[a]	3.29(5)	0.008(3)		

Sample ID	k-range	S_0^2	ΔE	CN ±25%	R(Å)	σ^2(Å^2)	χ^2_{red}	R factor
3-Mag								
V-O	2.5-10.5	0.949(7)	10.0(5)	3.97(6)	1.701(3)	0.01(1)	161	0.083
V-O-O MS				12.0[a]	3.175(6)	0.008(1)		
V-Fe				2.0(1)	3.33(3)	0.009(2)		
48-Mag								
V-O	2.5-10.5	0.95(1)	5.8(7)	3.1(2)	1.673(5)	0.009(1)	68	0.050
V-O				2.1(5)	2.24(2)	0.007(3)		
V-Fe1				0.90(3)	2.65(5)	0.009(3)		
V-O-O MS				12.0[a]	3.17(3)	0.007(1)		
V-Fe2				2.10(8)	3.31(1)	0.008(2)		
3-Sd-a								
V-O	3.0-10.5	0.95(1)	9.1(2)	1.89(5)	1.660(1)	0.004(1)	15	0.023
V-O				1.98(6)	1.96(2)	0.0086(9)		
V-Fe1				1.89(5)	3.36(5)	0.012(5)		
V-Fe2				1.1(4)	3.66(3)	0.006(4)		
3-Sd-b								
V-O	3.0-10.5	0.950(1)	6(2)	1.6(1)	1.651(6)	0.0020(9)	67	0.062
V-O				2.0(1)	1.95(1)	0.0084(8)		
V-Fe1				1.9(1)	3.31(4)	0.011(4)		
V-Fe2				1.0(3)	3.60(3)	0.006(4)		
48-Sd								
V-O	3.0-10.5	0.950(4)	3.7(6)	1.63(6)	1.662(9)	0.0011(4)	7	0.014
V-O				2.0(1)	1.95(1)	0.0064(8)		
V-Fe				1.95(5)	3.38(6)	0.016(2)		
3-Mck								
V-O	2.5-10.5	0.89(1)	-4.378(4)	1.1(2)	1.57(2)	0.0012(7)	148	0.104
V-S1				3.09(8)	2.16(2)	0.007(1)		
V-Fe1				1.48(8)	2.66(4)	0.007(1)		
V-Fe2				1.6(6)	2.91(4)	0.006(4)		
V-Fe3				3(2)	3.64(3)	0.009(3)		
V-S2				6.3(7)	4.38(5)	0.008(4)		
V-Fe4				4(2)	4.84(5)	0.005(4)		

Sample ID	k-range	S_0^2	ΔE	CN ±25%	R(Å)	σ^2(Å^2)	χ^2_{red}	R factor
48-Mck								
V-O	2.5-10.5	0.898(6)	-3.9(4)	0.8(2)	1.58(2)	0.001(1)	94	0.040
V-S1				3.17(6)	2.18(1)	0.006(1)		
V-Fe1				1.5(3)	2.66(4)	0.007(3)		
V-Fe2				2.0(7)	2.92(3)	0.007(3)		
V-Fe3				3.0(1)	3.58(4)	0.009(3)		
V-S2				7.2(2)	4.41(4)	0.010(4)		
V-Fe4				4(1)	4.90(8)	0.006(6)		
48-Fe^{2+}								
V-O	3.0-10.5	0.95(3)	4.8(4)	1.29(4)	1.660(4)	0.0019(3)	16	0.007
V-O				1.97(9)	1.955(7)	0.0083(5)		
V-Fe				1.8(2)	3.36(5)	0.0162(2)		

a Larsson et al. (2017)

b Besnardiere et al. (2016)

c Cooper et al. (2003)

d Krakowiak et l. (2012)

e Wen et al. (2016)

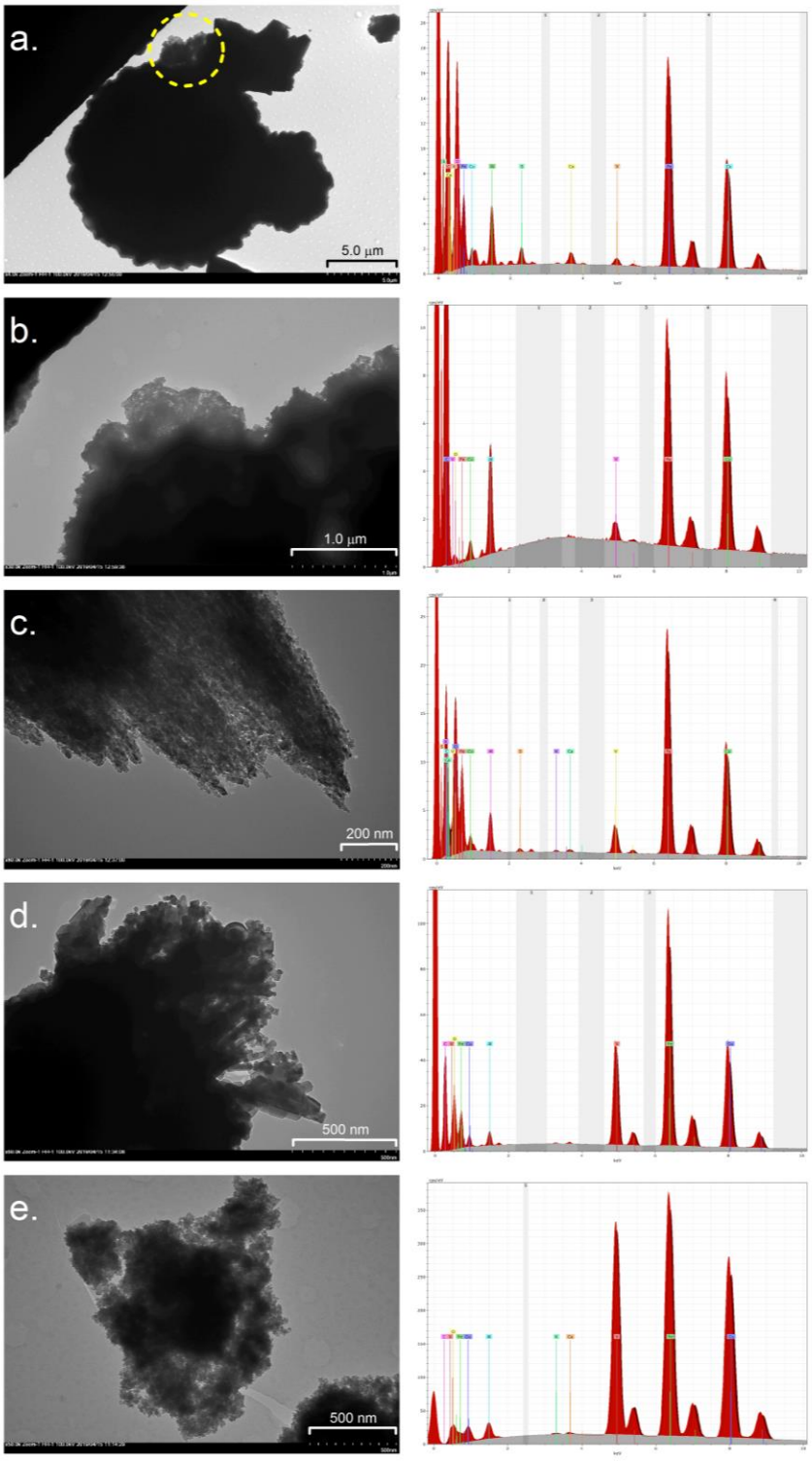

Figure A.3. TEM images (left) and corresponding EDX spectra (right) for reacted siderite (3-Sd and 48-Sd) (a, b, c) and secondary precipitates during aqueous Fe^{2+} (48-Fe^{2+}) reactions (d, e) Yellow circle in panel (a) highlights the image and EDX scan for panel (b).

Appendix B: Supplementary Information for Chapter 4

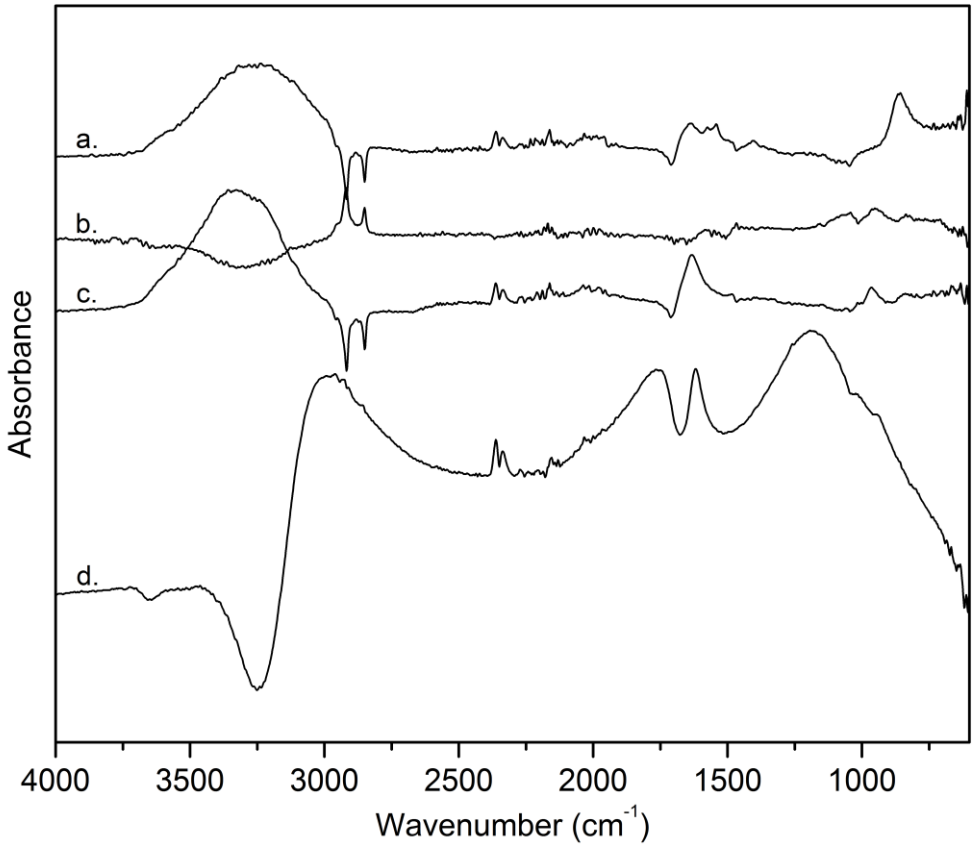

Figure B.1. Full ATR-FTIR spectra of aqueous V solutions (5000 µM) at pH 11 (a), 7 (b), 4 (c), and 1 (d) in 0.05 M NaCl.

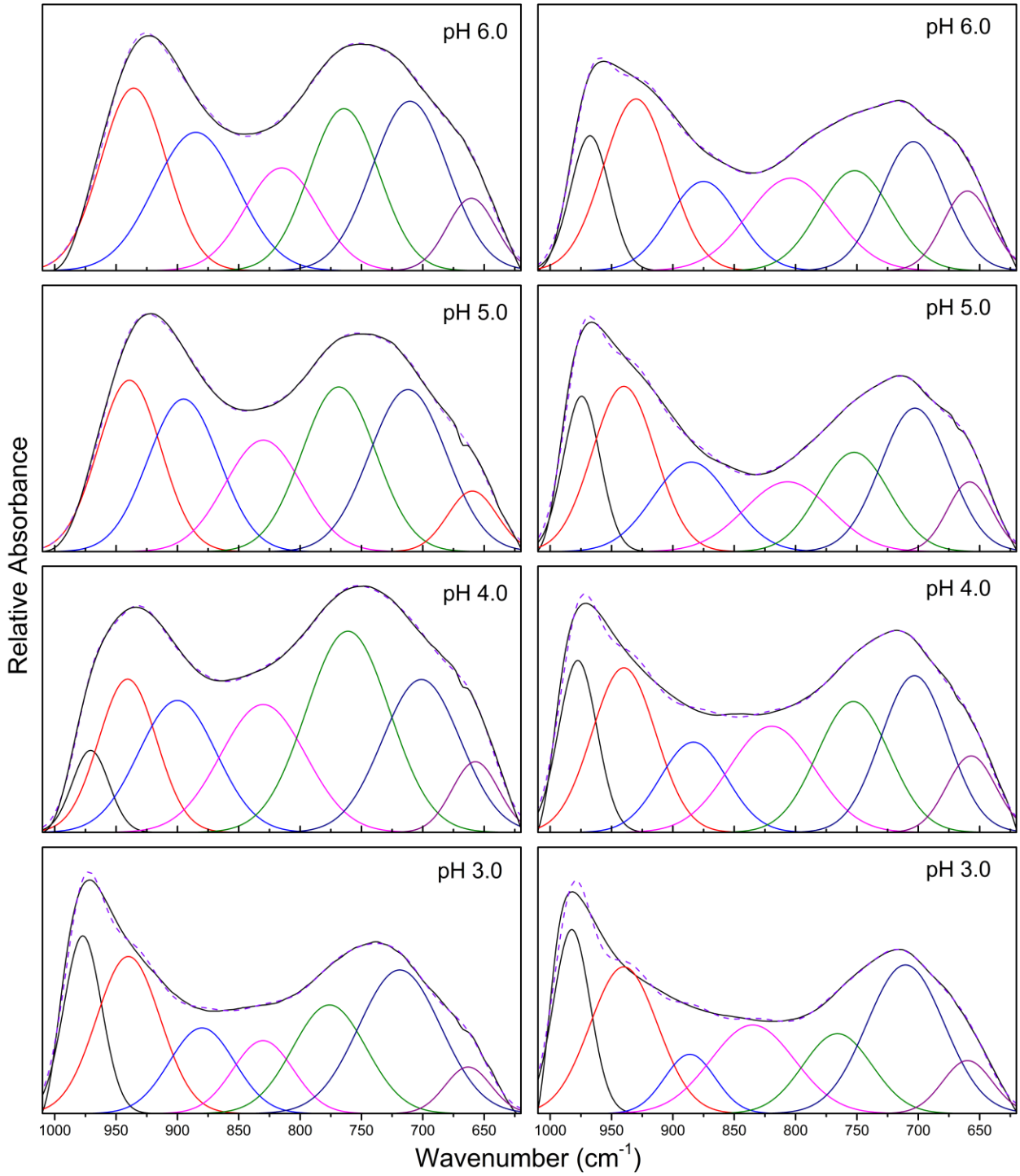

Figure B.2. ATR-FTIR spectra and decomposition fits of adsorbed V(V) onto ferrihydrite (left column) and hematite (right column) at 5000 µM. Black lines represent collected spectra and magenta dashed line is the simulated fit.

Table B.1. Summary of peak positions (cm^{-1}) and full-width at half-max (FWHM) (cm^{-1})for decomposition fits of V adsorption onto ferrihydrite and hematite from pH 3 to 6. Peak numbering increase with increasing band position. Goodness of fit represented by R^2 values.

Phase	pH	R^2		Peak 1	Peak 2	Peak 3	Peak 4	Peak 5	Peak 6	Peak 7
Ferrihydrite	6	0.998	Band Position	660	704	764	815	885	935	NA
			FWHM	40	62	57	60	68	53	NA
Ferrihydrite	5	0.999	Band Position	659	712	768	830	895	939	NA
			FWHM	40	63	60	62	58	51	NA
Ferrihydrite	4	0.999	Band Position	657	701	761	830	900	941	970
			FWHM	30	38	63	68	69	63	47
Ferrihydrite	3	0.993	Band Position	663	719	776	830	880	940	977
			FWHM	37	67	60	49	53	52	31
Hematite	6	0.998	Band Position	660	704	751	803	875	930	968
			FWHM	40	53	59	70	56	54	32
Hematite	5	0.996	Band Position	658	703	752	807	885	925	974
			FWHM	36	56	57	70	63	51	30
Hematite	4	0.991	Band Position	657	703	753	819	883	940	978
			FWHM	40	55	59	70	54	52	31
Hematite	3	0.982	Band Position	659	710	766	835	886	930	982
			FWHM	40	63	56	68	41	55	30

Table B.2. Fit summary for isotherm reactions onto hematite and ferrihydrite from pH 6 to 3. A_{max} represents the optimized maximum absorbance, K is the fit constant, and goodness of fit parameters, R^2 and RMSE.

	Hematite				Ferrihydrite			
pH	**6**	**5**	**4**	**3**	**6**	**5**	**4**	**3**
A_{max} (a.u.)	6.72	3.74	7.06	7.57	3.27	5.61	8.47	2.52
K (μM^{-1})	0.012	0.093	0.044	0.035	0.006	0.005	0.006	0.008
RMSE	0.027	0.031	0.063	0.027	0.043	0.057	0.045	0.037
R^2	0.983	0.764	0.694	0.951	0.973	0.959	0.971	0.974